The Astrophysical Journal, 896:79 (20pp), 2020 June 10 https://doi.org/10.3847/1538-4357/ab911e

HST Survey of the Orion Nebula Cluster in the H_2O 1.4 μm Absorption Band. I. A Census of Substellar and Planetary-mass Objects

Massimo Robberto[1,2], Mario Gennaro[1], Maria Giulia Ubeira Gabellini[3,4], Lynne A. Hillenbrand[5], Camilla Pacifici[1], Leonardo Ubeda[1], Morten Andersen[6], Travis Barman[7], Andrea Bellini[1], Nicola Da Rio[8], Selma E. de Mink[9,10], Giuseppe Lodato[3], Carlo Felice Manara[11], Imants Platais[2], Laurent Pueyo[1], Giovanni Maria Strampelli[1,2,12], Jonathan C. Tan[13,14], and L. Testi[11]

[1] Space Telescope Science Institute, 3700 San Martin Dr., Baltimore, MD 21218, USA[15]; robberto@stsci.edu
[2] Johns Hopkins University, 3400 N. Charles St., Baltimore, MD 21218, USA
[3] Dipartimento di Fisica, Università Degli Studi di Milano, Via Giovanni Celoria, 16, I-20133 Milano, MI, Italy
[4] European Southern Observatory, Karl-Schwarzschild-Str. 2, D-85784 Garching, Germany
[5] California Institute of Technology, MC 249-17, 1200 East California Blvd., Pasadena, CA 91125, USA
[6] Gemini Observatory, NSF's National Optical-Infrared Astronomy Research Laboratory, Casilla 603, La Serena, Chile
[7] Lunar and Planetary Laboratory, 1629 E. University Blvd., Tucson, AZ 85721-0092, USA
[8] University of Virginia, Department of Astronomy, P.O. Box 400325, 530 McCormick Rd., Charlottesville, VA 22904-4325, USA
[9] Center for Astrophysics, Harvard-Smithsonian, 60 Garden St., Cambridge, MA 02138, USA
[10] Anton Pannekoek Institute for Astronomy, University of Amsterdam, Science Park 904, 1098XH Amsterdam, The Netherlands
[11] European Southern Observatory, Karl-Schwarzschild-Str. 2, D-85748 Garching, Germany
[12] Department of Astrophysics, University of La Laguna, Av. Astrofísico Francisco Sánchez, E-38200 San Cristóbal de La Laguna, Tenerife, Canary Islands, Spain
[13] Department of Space, Earth & Environment, Chalmers University of Technology, Gothenburg, Sweden
[14] Department of Astronomy, University of Virginia, Charlottesville, VA 22904, USA
Received 2019 July 4; revised 2020 March 29; accepted 2020 March 30; published 2020 June 16

Abstract

In order to obtain a complete census of the stellar and substellar population, down to a few $M_{\rm Jup}$ in the ∼1 Myr old Orion Nebula Cluster, we used the infrared channel of the Wide Field Camera 3 of the Hubble Space Telescope with the F139M and F130N filters. These bandpasses correspond to the 1.4 μm H_2O absorption feature and an adjacent line-free continuum region. Out of 4504 detected sources, 3352 (about 75%) appear fainter than $m_{130} = 14$ (Vega mag) in the F130N filter, a brightness corresponding to the hydrogen-burning limit mass ($M \simeq 0.072\,M_{\odot}$) at ∼1 Myr. Of these, however, only 742 sources have a negative F130M–F139N color index, indicative of the presence of H_2O vapor in absorption, and can therefore be classified as bona fide M and L dwarfs, with effective temperatures $T \lesssim 2850$ K at an assumed 1 Myr cluster age. On our color–magnitude diagram (CMD), this population of sources with H_2O absorption appears clearly distinct from the larger background population of highly reddened stars and galaxies with positive F130M–F139N color index and can be traced down to the sensitivity limit of our survey, $m_{130} \simeq 21.5$, corresponding to a 1 Myr old ≃3 $M_{\rm Jup}$ planetary-mass object under about 2 mag of visual extinction. Theoretical models of the BT-Settl family predicting substellar isochrones of 1, 2, and 3 Myr down to ∼1 $M_{\rm Jup}$ fail to reproduce the observed H_2O color index at $M \lesssim 20\,M_{\rm Jup}$. We perform a Bayesian analysis to determine extinction, mass, and effective temperature of each substellar member of our sample, together with its membership probability.

Unified Astronomy Thesaurus concepts: Pre-main sequence stars (1290); Brown dwarfs (185); Young star clusters (1833)

Supporting material: machine-readable tables

1. Introduction

With ∼2000 members, the Orion Nebula Cluster (ONC) is the richest young (≃1–2 Myr) cluster within 2 kpc from the Sun (Lada & Lada 2003; Portegies Zwart et al. 2010). The cluster spans the full range of spectral types, from massive main-sequence OB-type stars to substellar brown dwarfs (BDs). Due to its modest distance from the Sun ($d \approx 400$ pc Großschedl et al. 2018; Kounkel et al. 2018) and to the relatively low foreground extinction ($A_V \sim 1$ Scandariato et al. 2011), the ONC can be studied in great detail. By characterizing the main parameters of the multitude of ONC pre-main-sequence stars, several studies have determined the main cluster properties, such as the structure, dynamics, star formation rate, and initial mass function (IMF). The reviews of Muench et al. (2008) and O'Dell et al. (2008) summarize the status of our knowledge before 2008. Further progress has been made in the past decade through photometric (e.g., da Rio et al. 2010, 2012; Andersen et al. 2011; Robberto et al. 2013; Drass et al. 2016) and spectroscopic surveys (e.g., Hillenbrand et al. 2013; Ingraham et al. 2014; da Rio et al. 2016).

Even if the ONC is usually regarded as the standard benchmark for comparative studies of young clusters, our knowledge of this system is not complete. Obtaining a complete census of the full population down to the minimum mass for opacity-limited fragmentation ($M \sim 1$–$10\,M_{\rm Jup}$; see Béjar & Martín 2018, and references therein) has not yet been achieved. One challenge is that the ONC is still partially embedded within its parental molecular cloud, carved by the ionizing radiation of the most massive stars, θ^1Ori-C in

[15] Based on observations made with the NASA/ESA Hubble Space Telescope, obtained at the Space Telescope Science Institute, which is operated by the Association of Universities for Research in Astronomy, Inc., under NASA contract NAS 5-26555. These observations are associated with program GO-13826.

particular. The molecular cloud provides a backdrop that mitigates background confusion, but its column density, and thus opacity, is not homogeneous (e.g., Scandariato et al. 2011; Kong et al. 2018): background objects can contaminate source counts, especially at infrared wavelengths, where the extinction is lower. Moreover, the side of the molecular cloud facing us is illuminated by the brightest ONC stars; the high surface brightness limits the sensitivity and completeness especially in the central regions where the cluster stellar density reaches its peak. The nonuniformity of the foreground extinction (Abel et al. 2019), the contamination from foreground pre-main-sequence (PMS) stars associated with older Orion associations (Bouy et al. 2014), the presence of circumstellar emission (proplyds, jets; e.g., O'dell & Wong 1996; Bally et al. 2000; Ricci et al. 2008), photospheric emission (accretion; e.g., Robberto et al. 2004; Manara et al. 2012), local extinction by envelopes and circumstellar disks with processed grains (Eisner et al. 2016), source variability (Herbst et al. 2002; Morales-Calderón et al. 2012), etc., hamper in many cases the capability of assigning a well-defined spectral type. Conventional imaging surveys carried out in broadband filters are effective at finding low-mass candidates, but firm separation from contaminants is problematic (Cook et al. 2017). Spectroscopic confirmation is generally needed to disentangle low-mass members against spurious contaminants.

Spectroscopic surveys of the ONC have identified about 60 BDs (Slesnick et al. 2004; Riddick et al. 2007; Weights et al. 2009), a relatively low number. Photometric studies (Hillenbrand & Carpenter 2000; da Rio et al. 2012) confirm that the population of low-mass sources is rather small. Other groups, however, find evidence of a rich BD population (Muench et al. 2002; Lucas et al. 2005; Drass et al. 2016).

To overcome the difficulty of determining the precise shape of the low-mass IMF, coarser diagnostics have been introduced. An often-used parameterization is the simple star/BD ratio R between the number of objects in the two mass bins from 0.08 to 1.0 $M_{\odot}$ and from 0.03 to 0.08 $M_{\odot}$. This has been adopted by Andersen et al. (2011), who analyzed Hubble Space Telescope (HST)/NICMOS data taken in the *JH* bands over a small ($\simeq$20%), noncontiguous fraction of the ONC field down to an unprecedented depth $H \sim 22$ (Robberto et al. 2013). They derived ratios ranging from $R = 3.7$ at the center down to $R \sim 1$ in the periphery, i.e., a significant depletion of substellar objects at the cluster core. At these faint sensitivity levels, however, contamination becomes a major issue, as broadband *JH* photometry cannot directly discriminate between cluster members and the multitude of background sources. In the case of the ONC, the accuracy of the correction applied to account for background contamination is limited by the nonuniformity of the nebular background, in terms of both brightness and extinction.

To avoid these limitations, da Rio et al. (2010, 2012) adopted a safer approach based on a direct measure of $T_{\rm eff}$. M dwarfs have been originally characterized by the onset of the molecular TiO absorption feature at visible wavelengths (Morgan et al. 1943). By using CCD photometry in the TiO molecular bands at $\sim$7700 Å, present in the atmosphere of PMS stars later than $\sim$M2 and BDs earlier than L2, Kirkpatrick et al. (1999) placed 1750 sources in the H-R diagram with minimal contamination from background sources, deriving a cluster IMF with a lower fraction of substellar objects than that found by Andersen et al. (2011). Observationally, the drawback in this case is that these observations were performed in the visible and from the ground. Therefore, they are not sensitive to the faintest and/or more embedded sources, in particular the low-mass tail of BDs and planetary-mass objects probed more efficiently, but with higher confusion, by Andersen et al. (2011).

The results of these two studies suggest that to firmly identify the substellar members of the ONC, it would be ideal to combine the strengths of the two methods: the depth of HST IR observations and the diagnostic power of an absorption feature sensitive to $T_{\rm eff}$ (and therefore to the mass) of very low mass objects. Najita et al. (2000) were able to determine the spectral type and reddening for every M-type star in the field of young cluster IC 348 using a photometric index based on the strength of the 1.9 μm water band. This feature was accessible at that time with the HST/NICMOS instrument but is beyond the spectral range of the more advanced HST/WFC3 that has superseded NICMOS. A similar feature that remains uniquely accessible by HST/WFC3 is the 1.345 μm H_2O absorption band that on the ground separates the *J* and *H* bands . The depth of the 1.345 μm band is known to correlate with $T_{\rm eff}$ in BDs (Jones et al. 1994; Delfosse et al. 1999, Figure 1) and remains prominent down to very low temperatures, $T_{\rm eff} \lesssim 500$ K, when the outer planetary atmospheres are cool enough to condense water vapor into clouds (Ackerman & Marley 2001; Burrows et al. 2003; Morley et al. 2014). According to the models, the F139M (covering the H_2O feature) and the F130N (adjacent continuum) filters of the Wide Field Camera 3 should provide a nearly reddening-free photometric index sensitive to $T_{\rm eff}$ (thus, a model-dependent mass) that at 6 $M_{\rm Jup}$ can be traced up to $A_V \simeq 40$ mag. This is because the H_2O index changes by just $\sim$0.023 mag/A_V, the two infrared bandpasses being close in wavelength. Due to its sensitivity to very cool objects, the H_2O index effectively discriminates young cluster members from reddened but intrinsically warmer background objects (Wallace et al. 2000; Gorlova et al. 2003).

In Section 2 we present the observations, detailing the survey strategy, data processing, and analysis and the final photometric catalog. In Section 3 we illustrate our completeness analysis. In Section 4 we present the main results, i.e., the capability of our measures to discriminate effectively between low-mass objects of the ONC and background stars, the relation between our water index and the effective temperature, the derived source parameters, and an analysis of the effect of contamination on the luminosity and mass functions. We present our strategy to overcome the limitation of the current models and derive a semiempirical isochrone in the two appendices. A full derivation of the ONC low-mass IMF, based on an extensive Bayesian analysis our our data, is presented in the second paper of this series by Gennaro & Robberto (2020, hereafter Paper II).

2. Observations

The data presented in this paper were obtained as part of the Cycle 22 HST Treasury Program "The Orion Nebula Cluster as a Paradigm of Star Formation" (GO-13826, P.I. M. Robberto). Observations were carried out between 2015 February 8 and November 29 using the ACS-WFC and WFC3-IR cameras in coordinated parallel mode. For the WFC3-IR survey we used the F139M and F130N filters.[16] The F139M filter (labeled as the H_2O/CH_4 filter in the WFC3 Instrument Handbook;

[16] The WFC3 data set, complemented by the ACS data from GO-10246 discussed in Section 5.7, is available in MAST at doi:110.17909/t9-7mhk-qp02.

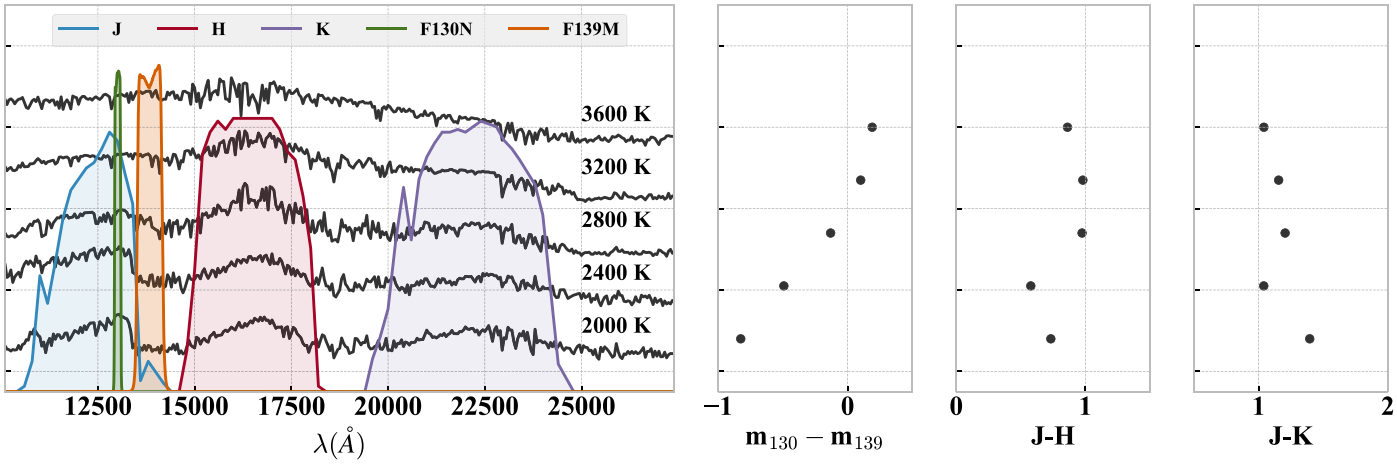

Figure 1. Left: theoretical near-IR spectra (BT-Settl) for five different values of $T_{\rm eff}$, with the transmission profiles of the broadband J, H, K bandpasses and our narrower F130N and F139M filters of WFC3. Right: color indices derived from our H_2O-sensitive filter combination of F130N−F139M, and from the $J-H$ and $H-K$ magnitude difference, for the same $T_{\rm eff}$ values assumed in the left panel (top to bottom: 3600, 3200, 2800, 2400, and 2000 K, roughly corresponding to $M = 0.7$, 0.2, 0.06, 0.015, and 0.006 $M_\odot$; see Appendix A). Surface gravities are $\log(g) \simeq 3.5$. The diagnostic power of the H_2O index is apparent from the systematic and large growth of the index toward cooler temperatures.

Dressel 2014) is a medium-band filter with central wavelength $\lambda_c = 1.383\ \mu$m and width $\Delta\lambda = 64.3$ nm. The F130N, nominally indicated as the Paschen-continuum filter, is a narrowband filter with $\lambda_c = 1.300\ \mu$m and $\Delta\lambda = 15.6$ nm. We adopted this filter, instead of the standard H_2O/CH_4-continuum F127M filter of WFC3, in order to measure the photospheric continuum without contamination from the $\lambda = 1.28\ \mu$m Paβ line, prominent in the Orion Nebula region.

2.1. Survey Strategy

Our observing strategy was driven by the goal of imaging with both cameras the same area covered by the 2005 ONC Treasury Program (HST GO-10246; Robberto et al. 2013) with adequate depth in the near-IR to identify all sources previously detected in the ACS F850LP filter. To facilitate the analysis of proper motion (I. Platais et al. 2020, in preparation), our original plan was to start each visit with the same pointing and orientation used by the first survey, replicating the exposures obtained 10 yr before with the same instrument and filter. In fact, since the tiling pattern used in 2005 had 50% overlap between visits, replicating only half of the original sequence of 104 visits was enough to cover the full field. In practice, various updates implemented to increase the accuracy of the HST guide star catalog have reduced the number of candidate guide stars in the Orion Nebula field. Therefore, for a number of pointings we could not find suitable guide stars. In order to cover those areas, we had to change the orientation of the telescope. This is the reason why 21 visits have roll angle different from the desired 100° or 280° and appear more randomly distributed on the otherwise regular mosaic pattern (see Figure 2).

Within each visit, corresponding to an HST orbit with about 45 minutes of target visibility, we maximized the WFC3-IR field coverage by taking four exposures per filter with large offsets; specifically, we pointed the telescope to the four vertices of a square with 120″ diagonal. This is the maximum distance allowed by the HST for a pointing maneuver that keeps a single guide star in use. The pointing overhead in this case is only 60 s; moving farther away forces the acquisition of a new guide star, which would require 6 minutes of overheads and strongly degrade the survey efficiency. The four pointings at the vertex of the inscribed square produce a square mosaic covering an area ∼2.8 times larger than the nominal WFC3-IR field of view, i.e., 13 arcmin^2 instead of the original 4.64 arcmin^2. About 35% of the field, in the central overlapping cross, is covered by two or more frames. Depending on the pointing, adjacent visits also have some degree of overlap, which increases the fraction of field covered at least twice.

With four dithered images in two filters per visit, our 52-visit WFC3-IR survey turns out to be composed of 416 individual images, covering overall a field of 0.135 deg^2.

The sequence of eight exposures per visit, with parameters listed in Table 1, alternates between the two filters to reduce the number of wheel moves. To pack eight ramps within a single orbit, we used SAMP-SEQ = SPARS100 with NSAMP = 4, corresponding to about 304 s of total integration time; however, two of the four exposures in the F130N filter had to be executed with SAMP-SEQ = SPARS50 and five frames, corresponding to about 204 s of integration time, in order to remain within the total duration of the visibility window.

2.2. Data Processing

Each image was initially processed using the standard WFC3 pipeline, which delivers count rate images corrected for flat-field and calibrated in units of electrons s^{-1} (suffix FLT). To derive the position of each source and reconstruct the full mosaic, the 416 images had to be distortion corrected, co-aligned, and placed at the absolute sky position, relying on the telescope offset information for the dithered exposures and on the ACS source catalog of Robberto et al. (2013) for the large-area mosaic.

We did not rely on the accuracy of the astrometric information in the native FITS headers released by the HST archive, as they were limited by the uncertainties on the absolute coordinates of the Guide Star Catalog and the accuracy and stability of the distance between the FGS guiders and the WFC3 focal plane. The astrometric information stored in the FITS header, therefore, was modified to recover the true absolute pointing of the telescope. We started with the images taken in the F139M filter, having higher signal-to-noise ratio,

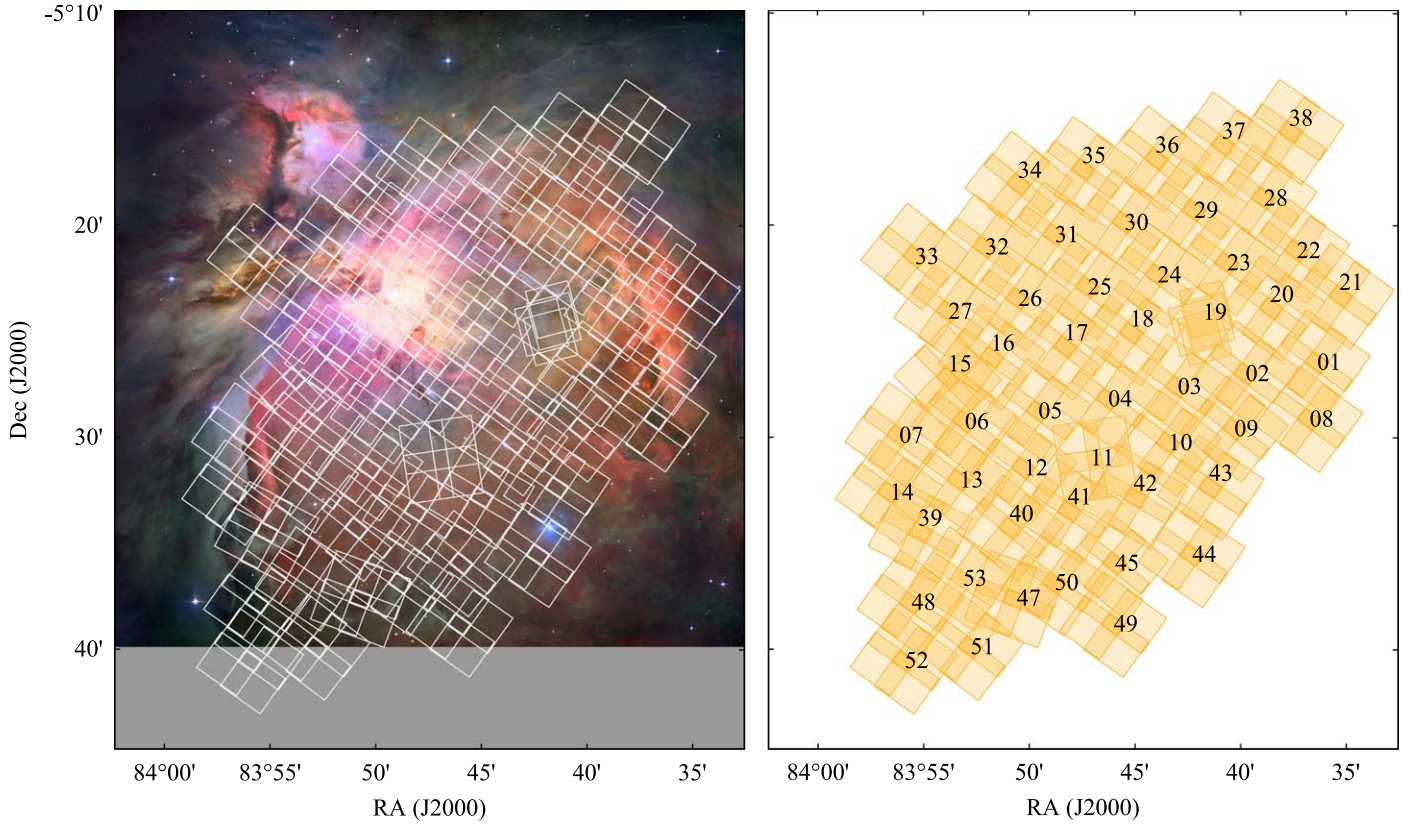

Figure 2. Field coverage of the HST GO-13826 observations presented in this paper. The large 2× dither pattern of each visit is apparent, together with the irregular configurations of the visits lacking suitable guide stars for nominal orientations.

Table 1
Observing Sequence per Visit

Filter	SAMP-SEQ	NSAMP	Exp. Time (s)	$\Delta X''$	$\Delta Y''$
F130N	SPARS100	4	303.933	0	0
F139M	SPARS100	4	303.933	0	0
F139M	SPARS100	4	303.933	0	120
F130N	SPARS100	4	303.933	0	120
F130N	SPARS50	5	203.934	60	60
F139M	SPARS100	4	303.933	60	60
F139M	SPARS100	4	303.933	−60	60
F130N	SPARS50	5	203.934	−60	60

Note. Column (1): HST/WFC3 filter denomination. Column (2): WFC timing sequence. Column (3): number of nondestructive samples per integration. Column (4): total exposure time per integration. Columns (5) and (6): typical commanded offset per dither move along the detector *X*- and *Y*-axes.

combining first the four images of each visit into single tiles. For this operation we relied on the relative offsets commanded to the telescope, executed with precision of a few milliarcseconds, since the four images had been taken using the same guide star. We thus produced 52 distortion-corrected tiles, each one a mosaic of 2 × 2 dithered frames.

The next step consisted in assigning to each tile the correct absolute astrometry, updating the WCS parameters stored in the FITS headers. To this purpose, we used the ACS source catalog of Robberto et al. (2013), as it provides a rich ($n = 2674$) and dense data set of sources detected in both the F775W ACS filter and our F139M filter. Each tile was thus registered with a relative accuracy of about 1/10 of an ACS pixel, or 5 mas. The absolute precision is limited by the accuracy of the ACS source catalog. A preliminary comparison with the GAIA coordinates shows discrepancies of the order of 50 mas or 1 ACS pixel, accurate enough for cross-matching against any other existing photometric catalog. An extensive astrometric analysis of the ACS data set based on Gaia DR2 coordiantes will be presented in I. Platais et al. (2020, in preparation).

Having registered our mosaic tiles on an absolute coordinate system, we used AstroDrizzle to create a full mosaic first in the F139M filter and then in the F130N mosaic by adopting the same astrometric information. The two mosaics in Figure 3 are therefore registered to each other with an accuracy of a few milliarseconds, or about 1/100 of a WFC3/IR pixel.

2.3. Photometry

We derived the photometry of each source using a combination of aperture and point-spread function (PSF) photometry. For PSF photometry we used DOLPHOT (Dolphin 2000), which uses a model PSF based on the HST TinyTim simulator (Krist et al. 2011). Since the HST PSF is not perfectly stable, DOLPHOT refines its shape in an iterative way, through comparison with the empirical one extracted from isolated stars in the field. This can be problematic in the case of the ONC, due to the presence of circumstellar structures, either in emission or in absorption such as photoionized proplyds, dark disks, and jets, as well as the scarcity of suitable sources in selected fields. For this reason, we paid special attention to parameters like the χ^2 returned by DOLPHOT to reject problematic sources. We found that in many cases the χ^2 values were worse for the F130N filter than for the F139M PSFs; this is probably due to the fact that the F139M PSFs are avaialble with a correction ("Anderson core") that is currently

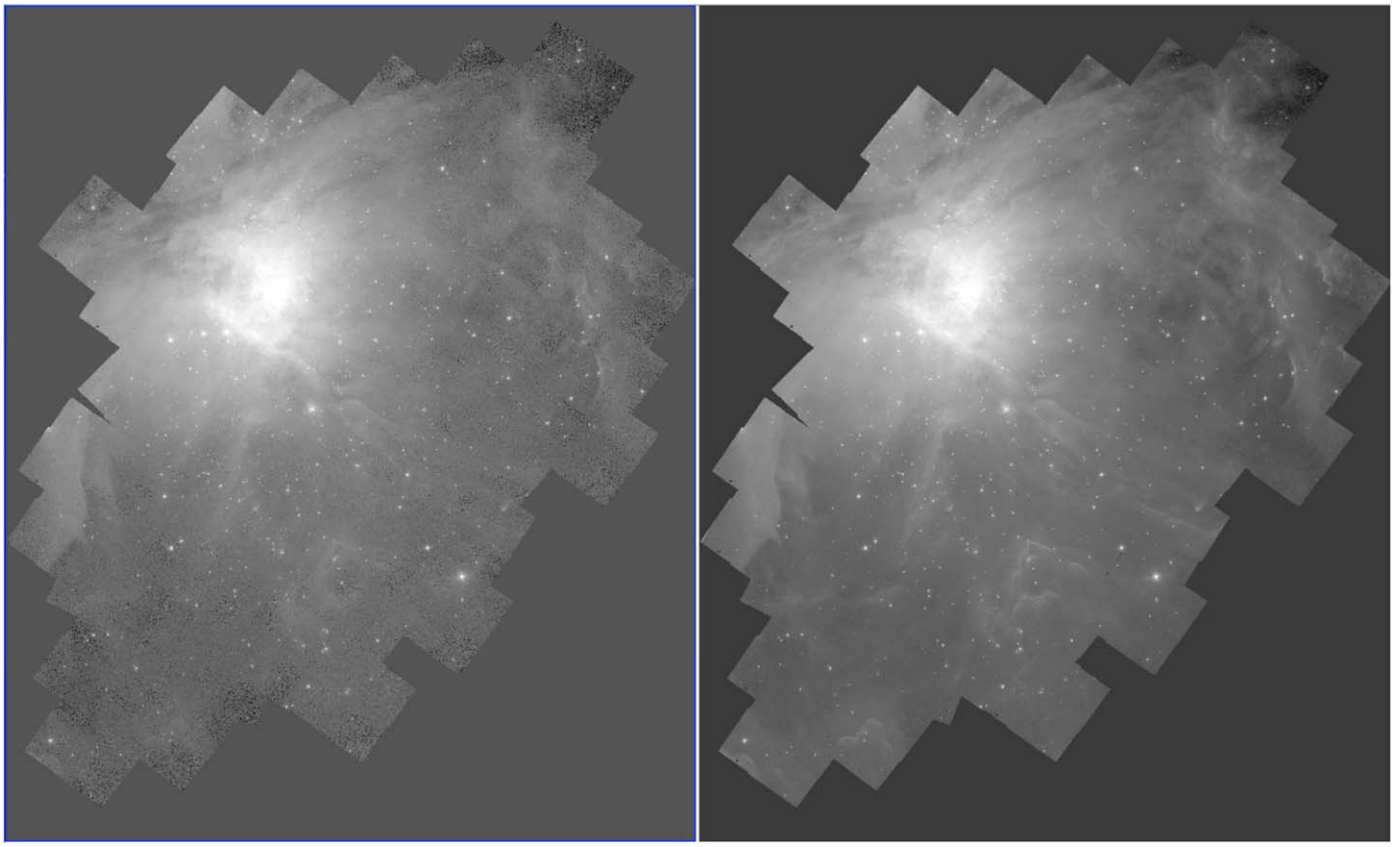

Figure 3. HST/WFC3-IR mosaics produced by our survey in the two filters F130N (left) and F139M (right). The two images, taken in adjacent bandpasses, are nearly indistinguishable except for the higher noise in the narrower F130N bandbass, as shown, e.g., in the lower part of the field. The Trapezium region is the saturated area in both images.

not available for the narrowband filter[17] (see, e.g., Dalcanton et al. 2012, for a discussion of the limitations of the TinyTim PSF models used for PSF photometry). Realizing that we could rely also on the more accurate but less precise aperture photometry, we adopted the general strategy of averaging multiaperture (3 and 15 pixels) and PSF photometry when the values were coincident within the errors and the reduced χ^2 of the PSF photometry was close to 1; otherwise, we used only aperture photometry. For the final photometric catalog, we averaged the values for the sources detected multiple times. Saturation starts to affect photometry at $m_{139} \simeq 9.5$ and $m_{130} \simeq 10.9$ (Vega magnitudes).

To reliably identify only real stars (point sources), we vetted the source catalog automatically created by DOLPHOT. After rejecting the sources having DOLPHOT parameters (sharpness, roundness, χ^2) and magnitude errors deviating from the median values of their magnitude bins by several sigmas, we performed a visual inspection of each source to uncover and reject residual artifacts such as the diffraction spikes produced by the brighter stars that DOLPHOT occasionally resolves in individual sources. We also rejected binaries found by DOLPHOT with separation $<0\farcs26$ (2 pixels), using in these cases only the values reported for the brightest source. A study of the binary population is the subject of Paper III of this series (Strampelli et al. 2020).

A last type of artifact we had to deal with is image persistence, which consists of the latent images of bright sources caused by the delayed release of trapped electrons in IR detectors (Smith et al. 2008). Assuming that persistence was affecting only the data taken within one orbit, meaning that at our flux levels the decay time is generally shorter than the duration of the Earth occultation, we flagged the pixels falling under the core of a bright star in each of the following exposures, so that the first pair (both filters) of exposures in an orbit was immune while the last pair was the most contaminated. Visual inspection at the expected positions showed that persistence artifacts were clearly present in our images, spread over the full field owing to the large dithers, but they had been almost totally rejected from our source catalog owing to the abnormal parameters of the PSF fitting, in both filters.

In Figure 4 we present the calibrated magnitudes versus their corresponding errors for our two filters. Our 5σ sensitivity limits ($dm \simeq 0.2$) are at about $m \simeq 21.5$, in both filters, with a larger scatter in the narrower F130N filter. At the faintest flux levels, large errors ($dm \gtrsim 0.35$) in the F130N filter are compatible with nondetection. The plot at the bottom shows the uncertainties in ($m_{139}-m_{130}$) color index, typically of the order of a few percent. In Figure 5 we show the spatial distribution of our sources with symbols coded according to their brightness and color. The blue sources show H_2O in absorption, and their distribution is generally centered around the Trapezium, consistent with this being a spectral signature characteristic of the cluster members, in the range of massess probed by our survey. The cyan-green sources do not show H_2O in absorption and are more uniformly distributed, with a

[17] See http://americano.dolphinsim.com/dolphot/ for the latest version of DOLPHOT code and tables.

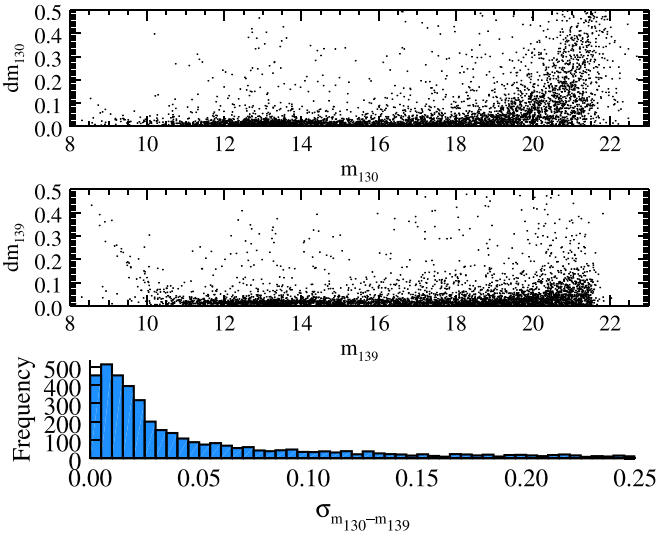

Figure 4. Magnitude error as a function of the m_{130} (top) and m_{139} (middle) magnitudes, and histogram of the uncertainties in the ($m_{130}-m_{139}$) color index (bottom).

surface density that tends to increase at the edges of the region. The red sources having high ($m_{139}-m_{130}$) color appear clustered, e.g., to the northeast of the Trapezium, in correspondence with the dark filament that delimits the Orion Nebula, compatible with highly reddened objects.

2.4. The Photometric Catalog

Our final catalog lists 4504 well-measured sources; of these, 137 appear saturated in the F130N filter and 221 in the broader F139M filter. Their brightness corresponds to sources with mass $\gtrsim$0.5 $M_{\odot}$, well above the mass range of interest; we include them in the catalog to facilitate cross-matching. The full list is presented in Table 2, providing, in this order, (1) entry number, from 1 to 4504; (2)–(3) R.A. and decl. (J2000); (4)–(5) (x, y) pixels in the final mosaic images, drizzled to a pixel scale of 0.″1285 pixel^{-1}; (6)–(7) magnitude and uncertainty in the F130N filter; (8)–(9) magnitude and uncertainty in the F139M filter; (10)–(11) ($m_{130}-m_{139}$) color index and uncertainty; and (12) number of detections for each filter.

3. Completeness Analysis

Artificial-star tests are a standard procedure to assess the level of completeness and precision of a photometric analysis. We performed our analysis using the capabilities implemented in the DOLPHOT package. The first step is to create a list of fake stars, and we generated 16,000 artificial stars. The (x , y) coordinates and the m_{130} magnitudes were randomly generated with uniform density distribution in the range 16–24 mag, while the m_{139} magnitudes were randomly generated from the cumulative distribution of the colors of the detected sources, for each magnitude bin. In this way the input magnitudes in the two filters reproduce the same range of colors covered by the data.

We then inserted sequentially on each visit the artificial stars, checking how many times DOLPHOT would retrieve them. Following DOLPHOT prescriptions, we adopted the same parameter files used for the real detections, with the following additional parameters appropriate for the artificial-star test: FakeMatch = 3.0 (maximum allowable distance in pixels between input and recovered artificial star), FakePSF = 1.5 (approximate FWHM of the artificial star in pixels), FakeStarPSF = 0 (in order to use the PSF residuals from the initial photometry run), FakePad = 0 (artificial stars will be considered only if their center falls within any of the images), and RandomFake = 1 (add Poisson noise to artificial stars).

Finally, we applied to the recovered artificial stars the same selection criteria used to automatically discard spurious detections in our source catalog. In particular, we rejected stars where the difference between the input and output magnitudes of the recovered artificial stars was higher than 0.75 mag in each filter. The final result was a series of tables showing, for each visit, the fraction of recovered artificial stars per bin of magnitude, i.e., a spatial map of the photometric completeness at each magnitude level. In general, completeness is dominated by the nebular background, as illustrated in Figure 6: in the central region ($r < 0.25$ pc angular distance from θ^1 Ori-C, or about 3% of our survey field), at the peak of the brightness of the nebular background, 50% completeness is reached in both filters at $m \simeq 18$. Moving away from the center, at projected distances larger than 1 pc, 50% completeness is reached at $m_{130} \simeq 21$ and $m_{139} \simeq 22$. Assuming the BT-Settl 1 Myr isochrone for the F139M filter, the average foreground extinction within our footprint ($A_V \sim 2.2$ mag, Scandariato et al. 2011), and a distance of 403 pc (Kuhn et al. 2019, see Appendix), we conclude that our observations are 50% complete down to about 10 $M_{\rm Jup}$ in the very central region and down to 2.5 $M_{\rm Jup}$ over 97% of our survey field.

4. Results

4.1. Color–Magnitude Diagram

In Figure 7 we present the CMD for all sources ($n = 450$). The data distribution shows a number of well-defined features. One can immediately recognize two main high-density populations: the clump at $m_{130} \sim 12$–14 and the redder sequence in the lower half of the diagram becoming increasingly denser as the magnitudes increase. The former is dominated by the main stellar population of the ONC, with masses around the peak of the IMF, in the 0.2–0.4 $M_{\odot}$ range; the latter is the main background population seen through the backdrop of the Orion Molecular Cloud (OMC), densest at faint magnitudes but with a tail toward brighter magnitudes of positive color. The bright, cluster member sequence also extends to fainter magnitudes but becomes increasingly displaced to negative index values. The lower half of the diagram at $m_{130} \lesssim 14$ thus shows two distinct populations: at the left of the main background population, one can recognize a second well-separated locus of sources that departs from the upper clump at $m_{130} \simeq 14$ and extends to the detection limit at $m_{130} \sim 21.5$, with increasingly bluer (negative) ($m_{130}-m_{139}$) color index. Negative color means that the 1.4 μm H_2O band is in absorption: we identify this sequence as the locus of the BD population of the ONC, and we count 742 sources with negative ($m_{130}-m_{139}$) color index.

At the very top of the diagram ($m_{130} \lesssim 11$), the brightest sources also display increasingly bluer colors: this is an artifact due to saturation, which in the broader F139M filter occurs at lower flux levels than in the F130N filter. The m_{130} magnitudes of these sources may still provide useful information, and therefore they have been kept in our catalog.

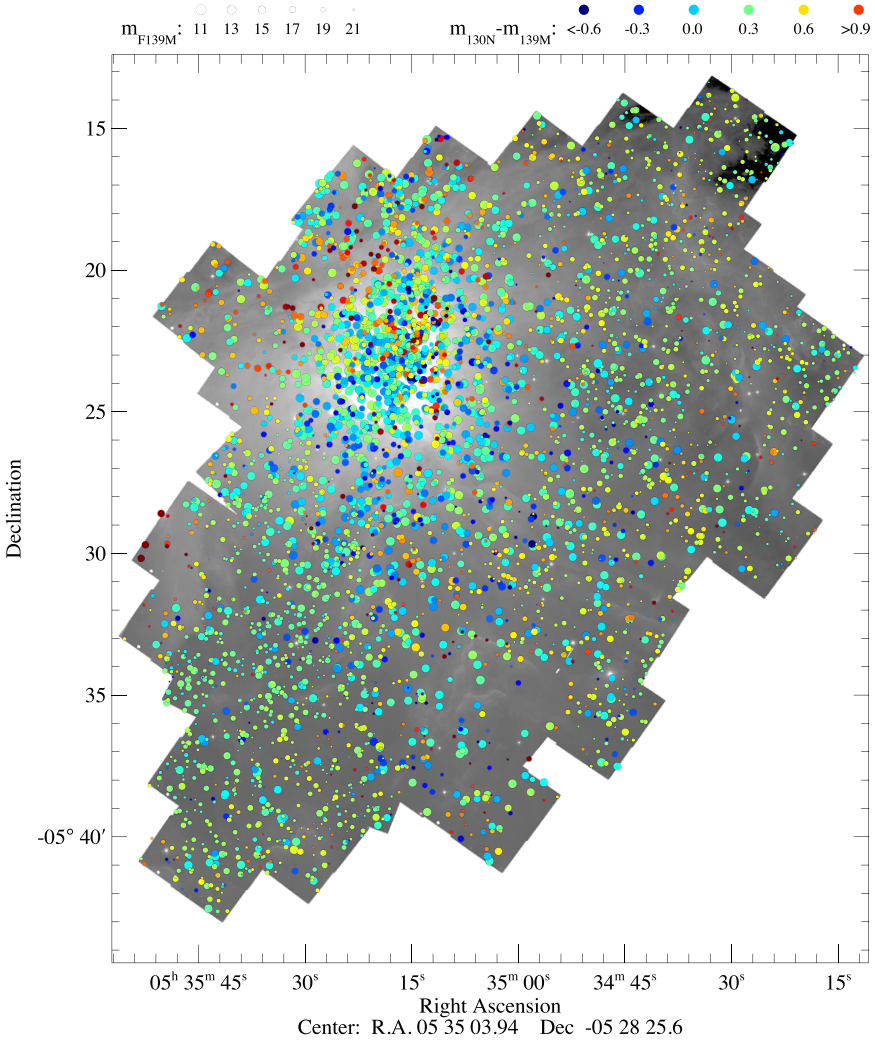

Figure 5. Survey area with the stars of our catalog superimposed. The symbol size scales with the magnitudes in the F139M filter, while the color encodes the $m_{130}-m_{139}$ color index, as indicated by the legend at the top of the figure.

Table 2
WFC3-IR Photometry of ONC Sources

ID #	R.A. (J2000)	Decl. (J2000)	x (pixels)	y (pixels)	m_{130} (mag)	dm_{130} (mag)	m_{139} (mag)	dm_{139} (mag)	color$_{130-139}$ (mag)	$d$color$_{130-m139}$) (mag)	Detections #
1	83.626381	−5.457797	10112.94	7947.76	<9.8	0.02	<9.78	0.20	−0.08	0.12	3
2	83.608998	−5.441777	10598.81	8397.33	<10.91	0.02	<10.67	0.03	0.24	0.02	4
3	83.616348	−5.442953	10393.41	8364.36	11.72	0.01	11.53	0.02	0.2	0.01	2
4	83.632944	−5.443575	9929.65	8347.02	12.15	0.03	12.13	0.01	0.03	0.02	2
5	83.617540	−5.444363	10360.07	8324.79	13.38	0.01	13.43	0.02	−0.05	0.02	2
…											

(This table is available in its entirety in machine-readable form.)

In Figure 7 we also plot the 1, 2, and 3 Myr isochrones taken from the BT-Settl model presented in Appendix A, scaled to a distance $d = 403$ pc, together with the points corresponding to the hydrogen- and deuterium-burning masses, assumed at $M = 0.072$ and $0.012\,M_{\odot}$, respectively, for solar metallicity (Chabrier & Baraffe 2000). The three curves are in good agreement with the data at $m_{130} \lesssim 15$, corresponding to about $0.045\,M_{\odot}$. Below this limit, however, there is a significant discrepancy, with the models predicting increasingly bluer colors, i.e., a deeper H_2O absorption feature down to $m_{130} \simeq 18$ (corresponding to about $0.01\,M_{\odot}$) and then a return to redder colors down to our sensitivity limit $m_{130} \simeq 21.5$ (which would correspond to 0.005–0.003 $M_{\odot}$ with about 2 visual magnitudes of reddening, depending on the assumed isochrone). For very low masses, therefore, it is not possible to directly use the theoretical predictions for our bandpasses in order to derive the main stellar parameters. In Section 4.9 we will present an empirical recalibration of the BT-Settle 1 Myr isochrone for $T_{\rm eff} \sim 2500$ K in our two filters, anchored to the HST/ACS visible broadband F850LP magnitudes and any

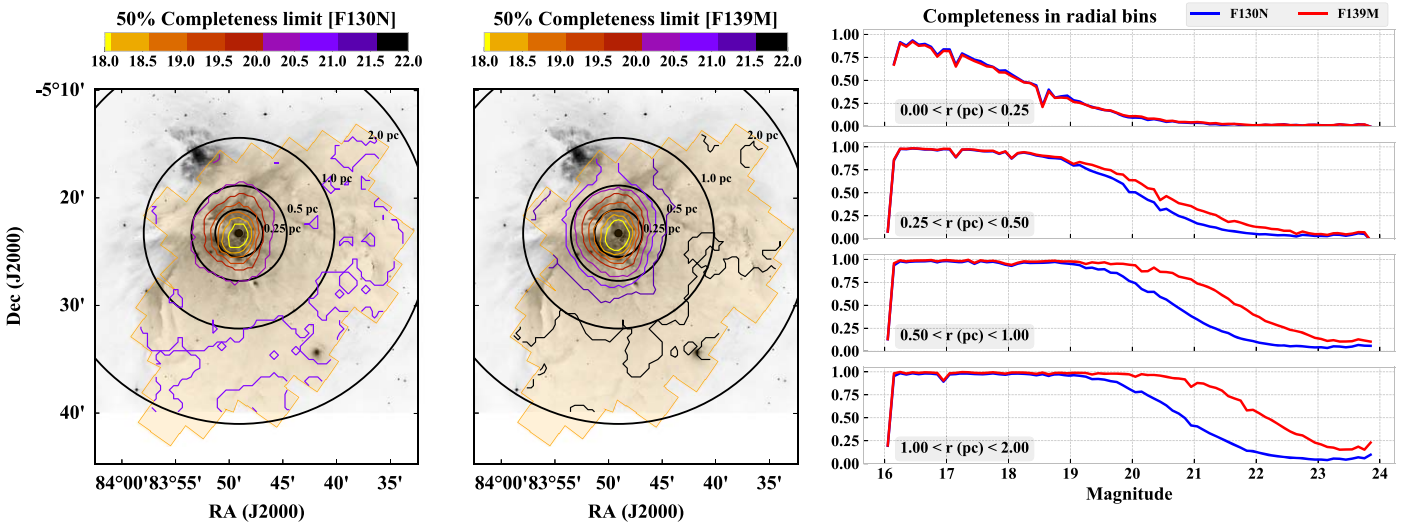

Figure 6. Spatial dependence of the completeness of our survey. The left and middle maps are relative to the F130N and F139M filters, respectively. The background image in gray scale is an optical image of the region. Overlaid in sepia is the footprint of our near-IR observations. The color contours show the 50% completeness limit in each band as a function of position in the sky. Their clustering at the center illustrates the rapid increase of completeness as one moves away from the bright cluster core. The black concentric circles, centered on (R.A., decl.)$_{J2000}$ = (05:35:16.26, −05:23:16.4), correspond to 0.25, 0.5, 1, and 2 pc from the cluster center. These radii are used to define the radial bins of the right panel, showing how the average completeness, plotted as a function of the input magnitude, increases moving away from the center.

prior information on membership and extinction. This requires an analysis of contamination, presented in the next three sections.

4.2. Galactic Contamination

We perform a semiquantitative assessment of galactic contamination using the Besançon model (Robin et al. 2003) of the Milky Way. The tunable parameters of the model were set as follows: distance interval from 0 to 50 kpc, to capture the full Milky Way disk, thick disk, and halo; field centered at Galactic coordinates ($l = 209\overset{\circ}{.}1$, $b = -19\overset{\circ}{.}5$) with an area of 0.135 deg^2, corresponding to the area of our survey; diffuse extinction was left at the nominal value (0.7 mag kpc^{-1}), as well as the range of stellar absolute magnitudes ($-7 < 20$) and spectral types (from O to OH/IR).

We additionally considered the extinction from the OMC. For all sources in the Besançon model with distance greater than the distance to the ONC of about 400 pc, we used the extinction map from Scandariato et al. (2011) to randomly assign a value of the total extinction A_V peculiar to the Orion Nebula, to be added to the values adopted by the Galactic model.

To derive magnitudes in our passbands, we used the noiseless apparent V magnitudes from the Besançon model and their diffuse A_V to obtain the absolute V magnitudes. We then use $T_{\rm eff}$, log g, and [Fe/H] from the model to assign a spectral energy distribution to the stars, using the `stsynphot` package.[18] For the spectral energy distributions, we adopted the Phoenix grid of models available in `stsynphot` (Husser et al. 2013). The spectra were normalized in flux using the absolute V magnitude, and then the total extinction (diffuse plus OMC, or diffuse only if $d < 403$ pc) was applied to the spectrum. Finally, the magnitudes in F130N and F139M were obtained by integration under the respective throughput curves, using the appropriate zero-points. Our artificial-star tests were then used to account for photometric errors using the spatially closest artificial stars, with input magnitudes within 0.1 mag from the Besançon model stars to allow for the usual underestimate of the photometric error in artificial-star tests.

The results are shown in Figure 8. The CMD shows that a few foreground main-sequence dwarfs (purple dots) do, in fact, lie within the locus of cluster members. The right panel of the figure, however, shows that their number is disproportionately low with respect to the bona fide members. Most of the background contaminants (blue dots) are very well separated from the sequence of low-mass cluster members, another demonstration of the effectiveness of our photometric water index. The histogram in the right panel also shows how the noise model we adopt (our artificial-star tests) is very effective in quantitatively predicting how many contaminants should be observable. The observed and simulated luminosity functions do match very well down to our detection limit.

4.3. Extragalactic Contamination

We also assess the amount of contamination to be expected from extragalactic sources. To do so, we adopt a very similar procedure to that described in Section 4.2 for the treatment of extinction and noise. The spectra, however, are derived from best fits to the multicolor photometry of all the sources available in the CANDELS fields catalogs (Koekemoer et al. 2011), using the procedure described in Pacifici et al. (2016). The five CANDELS fields provide a sampling of the expected cosmic variance between randomly selected fields. We normalize the numbers of observed galaxies using our survey area and the areas of each CANDELS field; then, we pick individual objects from the five fields at random and use their best-fit spectrum to synthetically determine the photometry in our bandpasses. The results are shown in Figure 8 as yellow dots.

Given that the best-fit template spectra used to fit the CANDELS HST photometry allow for a dependency on

[18] Available at https://stsynphot.readthedocs.io/en/latest/.

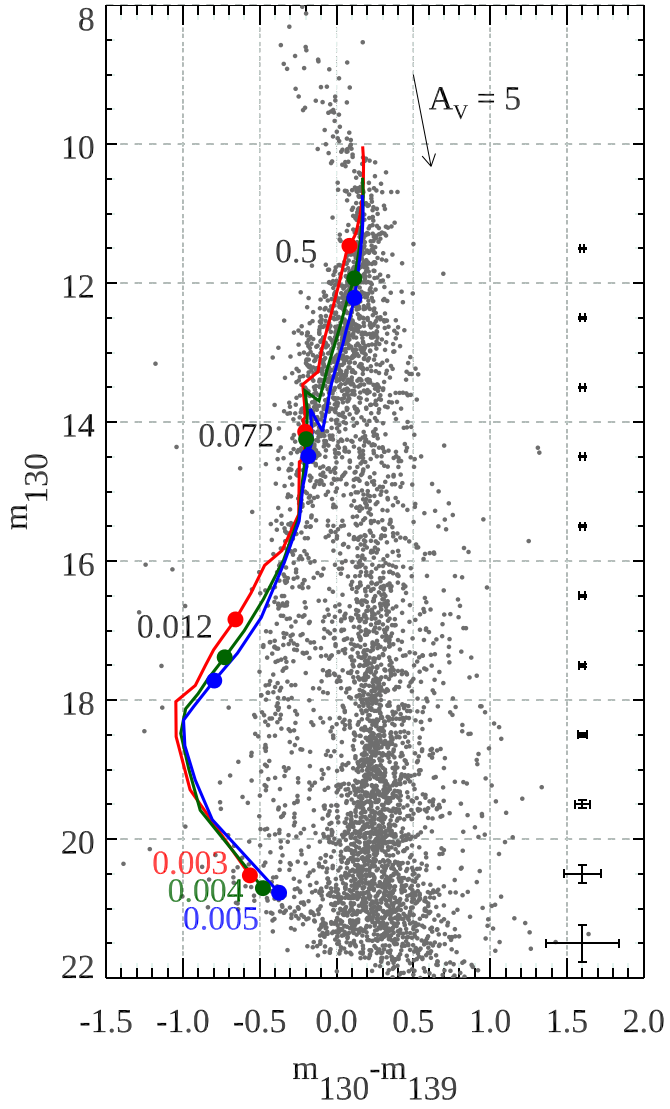

Figure 7. CMD for all sources detected in the F130N and F139M filters. The average photometric errors as a function of brightness are indicated on the right. The arrow indicates the reddening vector for $A_V = 5$ assuming the Cardelli et al. (1989) reddening law for $R_V = 3.1$. The three solid lines, top to bottom, represent the BT-Settl isochrones at 1 Myr (red), 2 Myr (green), and 3 Myr (blue). The filled dots on each isochrone correspond, top to bottom, to $M = 0.5$, 0.072, and 0.012 $M_\odot$ and 0.003, 0.004, and and 0.005 $M_\odot$, for the 1, 2, and 3 Myr isochrones, respectively.

redshift and star formation history, among other quantities, for some galaxies in the sample there can be strong emission lines in either one of the F130N and F139M bandpasses. Galaxies with strong lines in F130N will appear bluer than $m_{130}-m_{139} = 0$ in the figure; vice versa, the reddest objects may instead present emission lines in F139M. Most of the extragalactic sources, however, are generally undetectable at the depths of our observations; for clarity, in the figure we do not show those falling below our sensitivity limits. The large majority of observable extragalactic contaminants are relatively nearby galaxies dominated by stellar continuum emission in our passbands, and therefore they end up overlapping with the Galactic background stars in the CMD. Note that their number is far lower than background stars, in the magnitude ranged probed by our observations; these objects may be resolved by future high spatial resolution observations.

4.4. Contamination from Orion Foreground Population

Bouy et al. (2014) have found evidence for a foreground population in front of the Orion A cloud, deriving a distance of 380 pc and an age in the range of 5–10 Myr. It turns out that for our sample this population represents a negligible source of contamination. Out of the 605,020 sources contained in the full Bouy et al. (2014) catalog, 1573 fall within the boundary of our survey. After cross-matching with our catalog, we find 24 sources having both membership >99.5 (the criterion used by Bouy et al. 2014, to select foreground candidate members) and color $m_{130}-m_{139} < 0$. For 22 out of these 24 possible contaminants, the averages of the *J*- and *H*-band magnitudes are in the range of 12–14.5; this range (see our CMD) corresponds to the main stellar population of the ONC, where we count 670 sources with highest membership probability (Bayes factor = 2; see Section 4.10). The contaminant fraction is therefore of the order of 3%; the remaining two sources of Bouy et al. (2014) have fainter magnitudes and may contaminate our substellar population, traced down to planetary masses. But also in this case their number represents a negligible fraction. If the IMF maintains a negative slope going to even lower masses, it is safe to assume that the number of foreground contaminants remains extremely low also beyond the sensitivity limit probed by Bouy et al. (2014).

In conclusion, after considering all possible contamination from galactic, extragalactic, and foreground sources, our catalog of bona fide ONC members remains nicely uncontaminated, leading us to conclude that the large majority of sources with $m_{130} \gtrsim 14$ mag and $(m_{130}-m_{139}) < 0$ mag are likely to be ONC very low mass members. In Section 4.10 we will estimate the membership probability of each individual candidate on the basis of a Bayesian model of the cluster. This will require the assumption of a cluster isochrone for our two filters, as detailed in the following sections.

4.5. Comparison with Previous Spectral Classifications

To verify the accuracy of our photometric index, we have collected the spectral types presented by da Rio et al. (2012), complemented by the smaller catalogs (Slesnick et al. 2004; Riddick et al. 2007) of BD candidates, all converted to $T_{\rm eff}$ following Luhman et al. (2003). Discussing their more recent compilation of spectroscopically determined spectral types, Hillenbrand et al. (2013) point out that for early-type M stars some systematic discrepancy may be presented between their spectral types and those determined by da Rio et al. (2012) using narrowband photometry in the TiO bands, whereas for mid- to late M-type stars, the range probed by our survey, narrowband photometric methods are no less accurate on average than spectroscopic methods.

Using the published $T_{\rm eff}$ values, we can color-code the sources with known spectral type on the CMD diagram. Figure 9 shows how $T_{\rm eff}$ changes across the CMD, with the colored bands tracing the locus of the ONC. The large majority of points (circles) come from da Rio et al. (2012), whereas the spectroscopic surveys of Slesnick et al. (2004) (triangles) and Riddick et al. (2007) (squares) provide the effective temperature for the lowest-mass sources (blue colors). There is both a

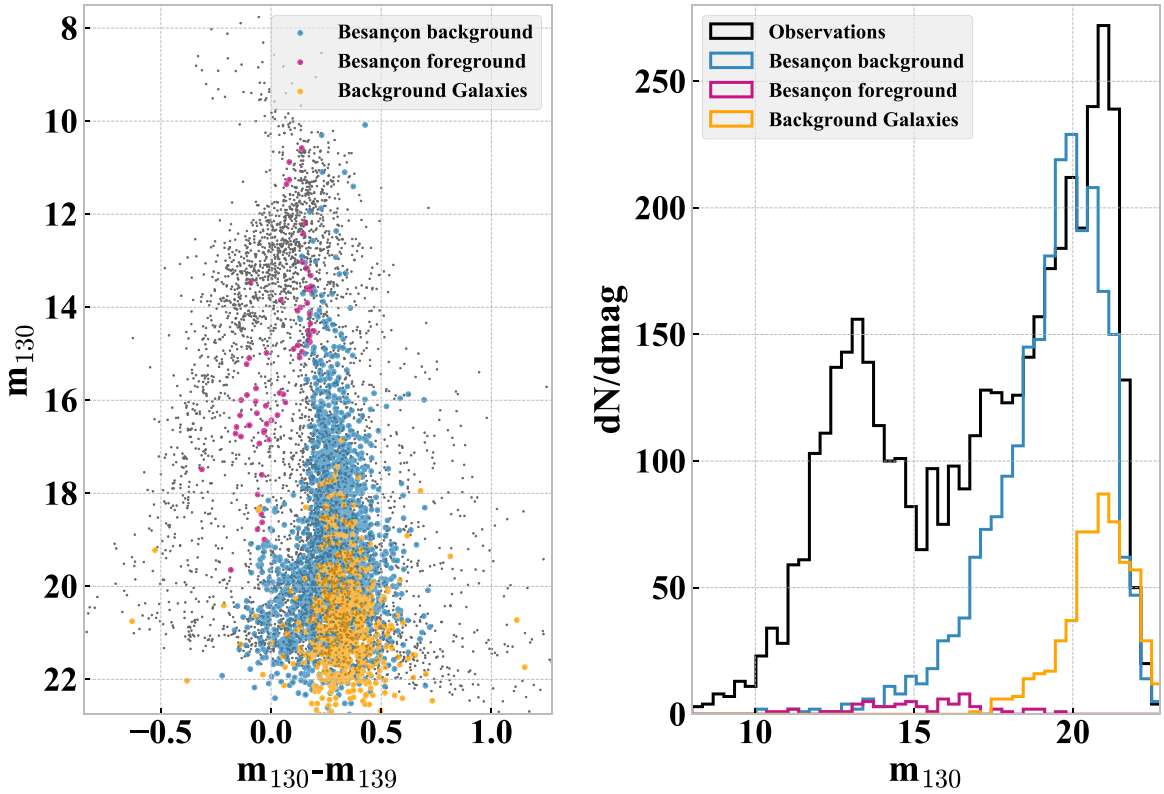

Figure 8. Contamination from stars, both foreground and background, and galaxies. Left: locus of the contaminants on the CMD; right: number distribution of the estimated population of contaminants vs. data.

substantial vertical spread and a clear correlation with the strength of the H_2O index when $T_{\rm eff} \lesssim 3200$ K.

Figure 9 shows how the large majority of sources belonging to the galactic population remain too faint for spectral classification owing to the large extinction from the OMC. It also shows the gain in sensitivity and diagnostic power achieved by our HST observations over previous surveys, as we are able to trace the substellar population of the cluster well beyond the $m_{130} \simeq 17$ equivalent limit reached by spectroscopic surveys; the majority of ONC sources fainter than $m_{130} \sim 15$ have no previously determined spectral type.

The color spread in Figure 9 cannot be entirely explained as the result of a narrow isochrone spread by random values of extinction. A similar plot for dereddened magnitudes (not shown here) would look quite similar to Figure 9, as expected since the median extinction of the sources with known spectral type is $A_V \simeq 2$ and about 90% of the sources are known to have $A_V \lesssim 5$ (da Rio et al. 2012). Instead, the vertical spread must be regarded as another indication of an intrinsic luminosity spread, confirming what was found by Reggiani et al. (2011) by analyzing HST photometry in visible bands, and inferred by Jeffries et al. (2011) through different age indicators.

4.6. An H_2O Spectral Classification Index

The sources with known spectral type allow us to derive a relation between $T_{\rm eff}$ and the intrinsic $(m_{130}-m_{139})$ color index, i.e., an H_2O spectral index. In Figure 10 we plot these two quantities, where the colors have been dereddened using the values of A_V provided by da Rio et al. (2012), Slesnick et al. (2004), and Riddick et al. (2007) and the following relations:

$$A_{130} = 0.264 A_V, \quad (1)$$

$$A_{139} = 0.241 A_V, \quad (2)$$

valid for the $R_V = 3.1$ Cardelli et al. (1989) reddening law. These relations have been derived using stsynphot (Laidler 2008) to extract synthetic photometry of late-type spectra, but using the values of A_V/A_λ at the effective wavelength of the filter provides nearly identical values, as we are dealing with relatively narrow filters.

The plot shows that our H_2O spectral index starts to be sensitive to $T_{\rm eff}$ below $\lesssim$3500 K; Given the scatter and low numbers at the bluest index values, we perform a basic outlier-resistant two-variable linear regression of all data with $T_{\rm eff} < 3500$ K (roughly corresponding to spectral type M2) and H_2O index > -0.3, deriving the following equation (solid line in Figure 10):

$$T_{\rm eff}\ ({\rm K}) = 3235 + 1020 \times (m_{130} - m_{139}), \quad (3)$$

with an average scatter around the best-fit line of 98 K. We also plot for comparison the 1–3 Myr isochrone from the BT-Settl models (see Appendix A) as a dashed line, which appears to systematically undestimate the effective temperature below $T_{\rm eff} \sim 3000$ K. As remarked by da Rio et al. (2012), the presence of accretion would create veiling of the spectral signatures, reducing the measured depth of the 1.4 μm absorption feature and therefore producing an H_2O index redder than the pure stellar isochrone; this implies that the discrepancy between the model and our observations cannot be

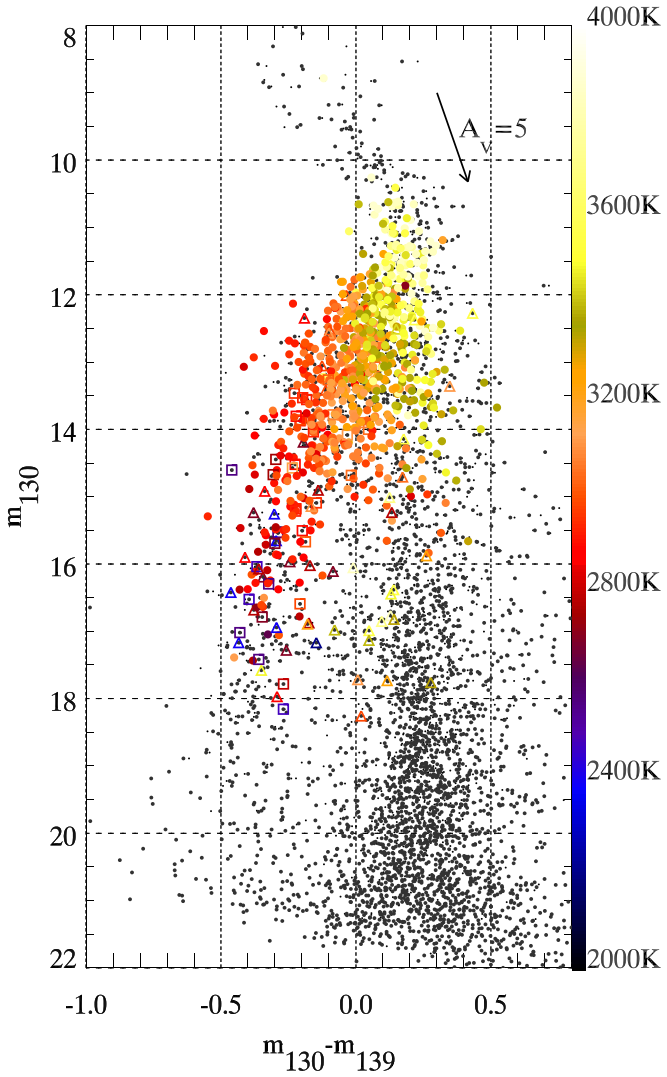

Figure 9. CMD highlighting sources that are known cluster members with determined effective temperature. The colors are coded according to the temperature scale presented on the right axis. The symbols label the different source catalogs: circles for da Rio et al. (2012), triangles for Slesnick et al. (2004), squares for Riddick et al. (2007).

reconciled by assuming some unaccounted contribution from extra accretion luminosity.

4.7. Stars with ACS Detection in the F850LP Filter

Using the source catalog obtained from our 2005 HST Treasury Program GO-10246 (Robberto et al. 2013), we combine our near-IR WFC3 data with previous ACS photometry at visible wavelengths. The deepest optical data have been obtained with the F775W filter and, especially, in the long-pass filter F850LP.

Cross-matching the two catalogs by assuming a maximum distance of 0.″2 between the celestial coordinates, we find that 2753 ACS sources have been also detected in our near-IR bands. The combined photometry is presented in Table 3. As shown in Figure 11, the sources detected with both ACS and WFC3 are evenly distributed across our near-IR CMD. Overall, the depths of the two HST Treasury programs on the Orion Nebula, GO-10246 and GO-13826, are comparable, meeting our original survey requirements.

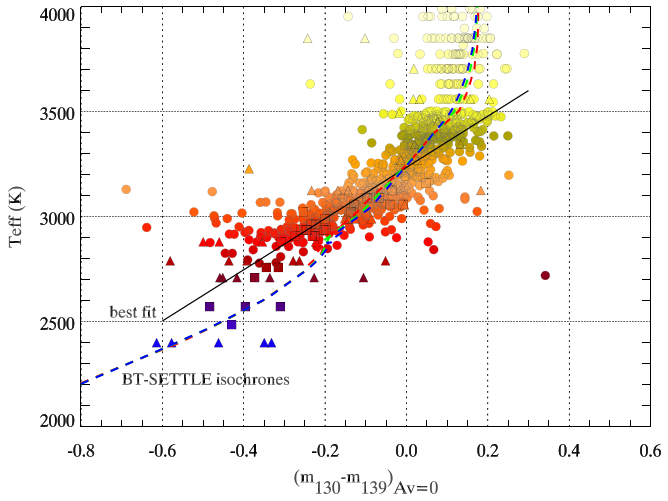

Figure 10. Relation between the effective temperatures reported in the literature and our H_2O index. The symbols and color scale are the same as in Figure 9. The red, green, and blue dashed lines, barely distinguishable, refer to the 1, 2, and 3 Myr isochrone of the BT-Settl models. The solid line represent the best linear fit to the data (see text).

With a third photometric band, we can create a distance-independent ($m_{850}-m_{130}$) versus ($m_{130}-m_{139}$) color–color diagram, shown in Figure 12, analogous to the (753 − *I*) versus (753–770) diagram presented by da Rio et al. (2012) for the 6100 Å TiO band. The plot shows again the decrease in $T_{\rm eff}$ as one moves leftward to bluer color indices. The spread along the reddening vector also decreases, consistent with the fact that fewer very low temperature and fainter objects have been identified and classified. For spectral indices ($m_{130}-m_{139}$) $\gtrsim$ 0.2, the 1 Myr BT-Settl model isochrone (dashed line) nicely matches the lower envelope of the data distribution, i.e., the locus of the dereddened sources. Beyond this value, the model isochrone predicts lower $m_{850}-m_{130}$ color index, another indication of the current limits of the models in our passbands. At the right side of the plot, many sources with high reddening have no spectral type: these are faint, highly reddened background stars.

Following da Rio et al. (2012), we have slightly modified the isochrone to make sure that it matches more precisely the lower envelope of the data points. We match the theoretical isochrone above ($m_{130}-m_{139}$) = −0.2, corresponding to the location of a 0.07 $M_\odot$ star in the 1 Myr uncorrected BT-Settl isochrone. For bluer colors and smaller masses, our line departs sligthly from the model. The black solid line in Figure 12 is given by the equation

$$m_{130} = A \times (m_{130} - m_{139}) + (m_{850} + B), \qquad (4)$$

where $A = 2.7$, $B = -0.85$ when ($m_{130}-m_{139}$) > −0.2 and $A = 1.38$, $B = -1.13$ below this value. This equation sets a first constraint on the source colors that we will use in the next section to refine the cluster isochrone in our CMD.

Ideally, it should be possible to derive the extinction A_V of each source in this diagram by projecting the data point on the isochrone. However, since the ACS F850LP data and the present WFC3 observations were taken at different epochs, the results would be affected by stellar variability. According to Herbst et al. (2002), essentially every ONC star brighter than $m_I = 16$ is variable, with about 50% having peak-to-peak variations ∼0.2 mag or more in the Cousins *I* band. A change of 0.2 mag in our near-IR filters would correspond to an error

Table 3
Cross-matched ACS-VIS and WFC3-IR Photometry of ONC Sources

Index	R.A. (J2000) (deg)	Decl. (J2000) (deg)	m_{775}[a] (mag)	dm_{775}[a] (mag)	m_{850}[a] (mag)	dm_{850}[a] (mag)	m_{130} (mag)	dm_{130} (mag)	m_{139} (mag)	dm_{139} (mag)	color$_{130-139}$ (mag)	$d$color$_{130-139}$ (mag)
3	83.61634780	−5.44295295	14.249	99.990	13.414	99.990	11.724	0.011	11.530	0.018	0.195	0.007
4	83.63294382	−5.44357471	14.434	99.990	13.567	99.990	12.146	0.030	12.132	0.012	0.031	0.021
5	83.61754036	−5.44436287	16.037	0.002	14.901	0.002	13.378	0.010	13.427	0.023	−0.053	0.018
7	83.62495811	−5.42146638	15.662	0.002	14.705	0.002	13.228	0.013	13.309	0.014	−0.093	0.016
…												

Note.
[a] In order to account for variability, Table 5 of Robberto et al. (2013) reports the magnitudes of each individual detection. To compile this table, we have taken the average magnitudes when multiple values have been reported. Following the same convention adopted by Robberto et al. (2013), a magnitude value equal to 99.99 indicates a value below the detection limit reported in the adjacent column for the magnitude error. Vice versa, a magnitude error equal to 99.99 refers to a saturated star brighter than the magnitude reported in the corresponding column for the source magnitude.

(This table is available in its entirety in machine-readable form.)

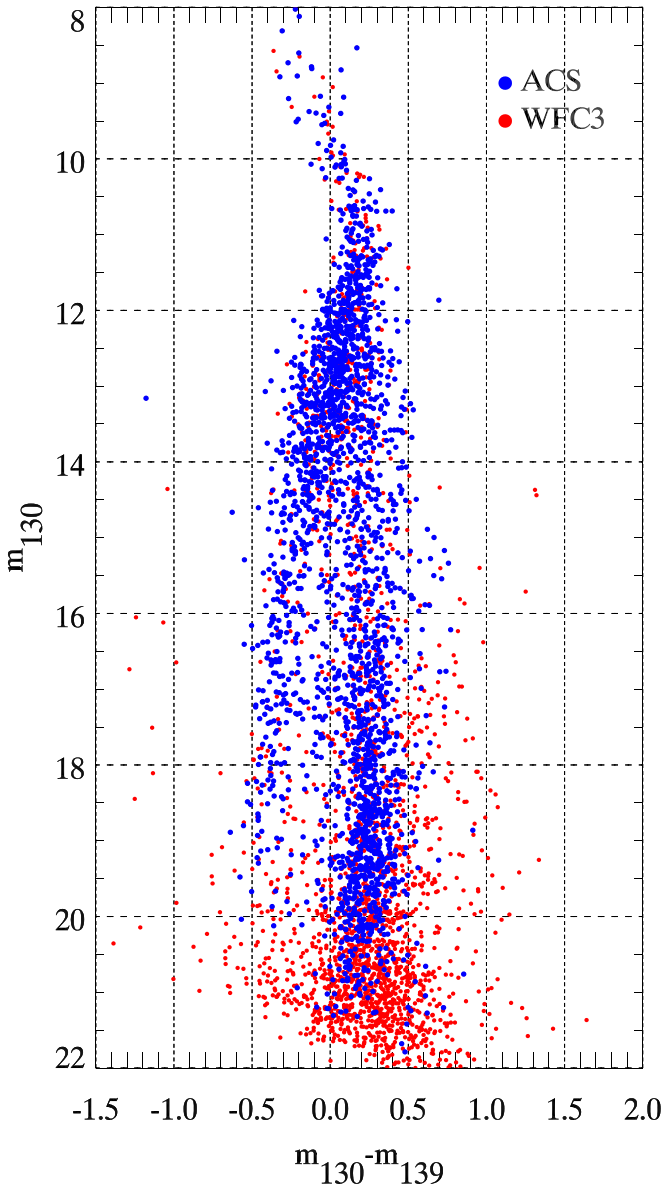

Figure 11. WFC3-IR CMD, with sources detected in the F850LP filter overplotted as blue dots.

in the estimated value of A_V of 0.8 mag. In general, simultaneous wide-band measures are needed to reliably estimate the extinction toward individual young stars, and consequently all derived stellar parameters like luminosity, radius, isochronal age, and mass.

4.8. Veiling

Veiling from mass accretion may potentially affect our color index. To assess its relevance, we can refer to Mohanty et al. (2005), who show that the mass accretion rate in young ultra −low-mass objects down to nearly the deuterium-burning limit appears on average to decrease steeply with mass, e.g., $\dot{M} \propto M^{-2}$. Below the H-burning limit, $\dot{M}$ values are typically range from 10^{-11} to $10^{-12}\,M_\odot\,\mathrm{yr}^{-1}$. If we take as a reference a $0.07\,M_\odot$ star and compare the accretion luminosity versus bolometric luminosity from the BT-Settl model for a 1 Myr isochrone, we have accretion luminosities of the order of 10^{-4} the bolometric luminosity of the BD, extremely small. Moreover, the peak of ≃2500 K stellar spectra falls in the near-IR, where the H_2O feature is prominently observed; vice versa, accretion continuum is generally approximated as a ∼10,000 K blackbody plus emission lines. Both factors, total luminosity and spectral distribution, allow us to conclude that the contribution of accretion veiling in our data is expected to be negligible.

4.9. Isochrone

A direct comparison of our data set with the theoretical isochrone, as presented in Figures 7 and 12, clearly shows that a BT-Settl model predicting the H_2O color down to planetary masses does not agree with the observations below $T_{\rm eff} \sim 2500$ K. The causes of the discrepancy in the F139M band may be related to the line lists and opacity tables used to predict the water absorption feature at low effective temperatures. In fact, the data we are presenting are the first to provide a sample large enough to unveil systematic differences between theory and observations in near-IR bands not accessible from the ground. This type of data set may thus help constrain theoretical predictions of the near-IR spectra of young BDs and planetary-mass objects.

Table 4
Estimated Parameters of the ONC Sample

Index	log(Bayes Factor)	Mass ($M_\odot$)	$T_{\rm eff}$ (K)	A_V (mag)
1	2.00	0.91	3757	−3.62
3	2.00	0.81	3678	3.30
4	2.00	0.28	3266	0.12
5	2.00	0.14	3084	1.7
...	...	...	...	...

(This table is available in its entirety in machine-readable form.)

In order to provide an initial raw estimate of the physical parameters of our very low luminosity sources, we apply an empirical correction to the model predictions in our IR bandpasses using the observational constraints inferred from both the near-IR CMD (Figure 11) and the color–color diagram built combining ACS and IR data (Figure 12). Our goal is to shift the theoretical isochrone in our CMD toward an empirical locus that better describes the average location of the ONC stars. Our corrections modify the model predictions for our two IR bands, but not for the broadband F850LP filter, and it is not arbitrary, being constrained by the relation between (m_{850}, m_{130}) and m_{139} determined with the color–color diagram (Equation (4)): our adjusted empirical IR isochrone, when plotted in the color–color diagram, must still lie along the lower envelope of the data points, i.e., the envelope corresponding to stars with $A_V = 0$. The models correctly predict the m_{850} magnitudes, which we leave unchanged, while a correction is provided in both the m_{139} magnitude and the ($m_{130}-m_{139}$) color index. In the Appendix we describe in detail the process used to derive our empirical correction. Table A1 lists the corrections as a function of $T_{\rm eff}$ along the isochrone. In this way the correction, which is derived using the 1 Myr isochrone, can be applied to other isochrones, assuming that the observed discrepancies are a function of the model temperature only.

4.10. Membership Probability

In order to quantify the probability of each source in our catalog to be either a cluster member or a background contaminant, we calculate the ratio of the marginal likelihood of our data given these two hypotheses. The results for an individual star, characterized by its color and magnitude measurements arranged in a 3-elements vector $\boldsymbol{d}_i$, are expressed in terms of the Bayes factor, given by

$$\mathrm{BF}_i = \frac{p(\boldsymbol{d}_i|ONC)}{p(\boldsymbol{d}_i|\overline{ONC})}. \quad (5)$$

A Bayes factor BF = 1 indicates equal probability of a star being a cluster or background source. The marginal likelihood for the membership hypothesis, $p(\boldsymbol{d}_i|ONC)$, is obtained by marginalizing over a model of the CMD for the ONC, while the likelihood for the nonmember case, $p(\boldsymbol{d}_i|\overline{ONC})$, is marginalized over a model of the CMD for background contaminants. The procedure for marginalization follows the scheme by Ruffio et al. (2018).

The cluster model adopted here is described in detail in the accompanying Paper II on the ONC IMF, so here we only summarize the main points. We describe the CMD of the ONC population using the 1 Myr isochrone derived in the previous section. The mass distribution is described as a three-part broken power law, similar to the Kroupa (2001) IMF, the parameters of which are determined in Paper II. To populate the cluster CMD model, we draw a parameter set from the IMF posterior and use such parameters, which include a normalization factor and a value for the binary fraction, to draw a given number of masses. Using the 1 Myr isochrone, we assign a color and a magnitude value to each mass. We also draw on-sky positions according to the 3D model of the ONC also described in Paper II (a spherically symmetric model with a radial density profile declining like a power law, a model that reproduces very well the observed radial counts profile). Positions and intrinsic magnitudes, together with the reddening map by Scandariato et al. (2011) and the artificial-star tests, allow us to produce a realistic CMD for a model-ONC, which includes measurement errors and incompleteness. The experiment is repeated by drawing multiple IMF parameter sets, thus marginalizing over the posterior distribution of IMF parameters, until 2 million stars are drawn. The model probability is then derived by using a kernel density estimate, in CMD space, which is normalized to unity over the entire CMD. A similar approach is used for the background. In this case, the simulated CMD is derived from the union of the Besançon model, for galactic contaminants, and an estimate of the extragalactic contaminants using the CANDELS fields (see Sections 4.2 and 4.3). The cardinality of the ONC and $\overline{ONC}$ CMD model priors are based on the number of cluster sources identified based on a simple color-cut argument and the number of expected background sources from the Besançon model and the area-scaled CANDELS counts.

Our results are shown in Figure 13 and are broadly in line with the more cursory color-based approach. Our threshold for declaring a source an ONC candidate, i.e., showing some evidence that it may not belong to the background population,

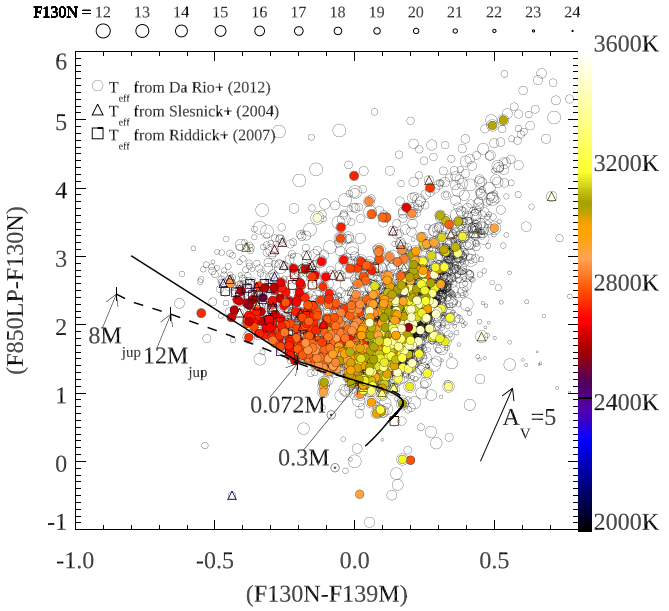

Figure 12. $m_{850}-m_{130}$ vs. $m_{130}-m_{139}$ color–color diagram showing the distribution of sources with known spectral type (color-coded accrording to the temperature scale presented on the right axis) and unknown spectral types (gray open circles); the size of the circles is indicative of the source brightness in the F130N filter, according to the scale presented on the top axis. The dashed line indicates the locus of the BT-Settl 1 Myr isochrone. The solid line is our slighlty revised line better matching the envelope of the data points at low masses.

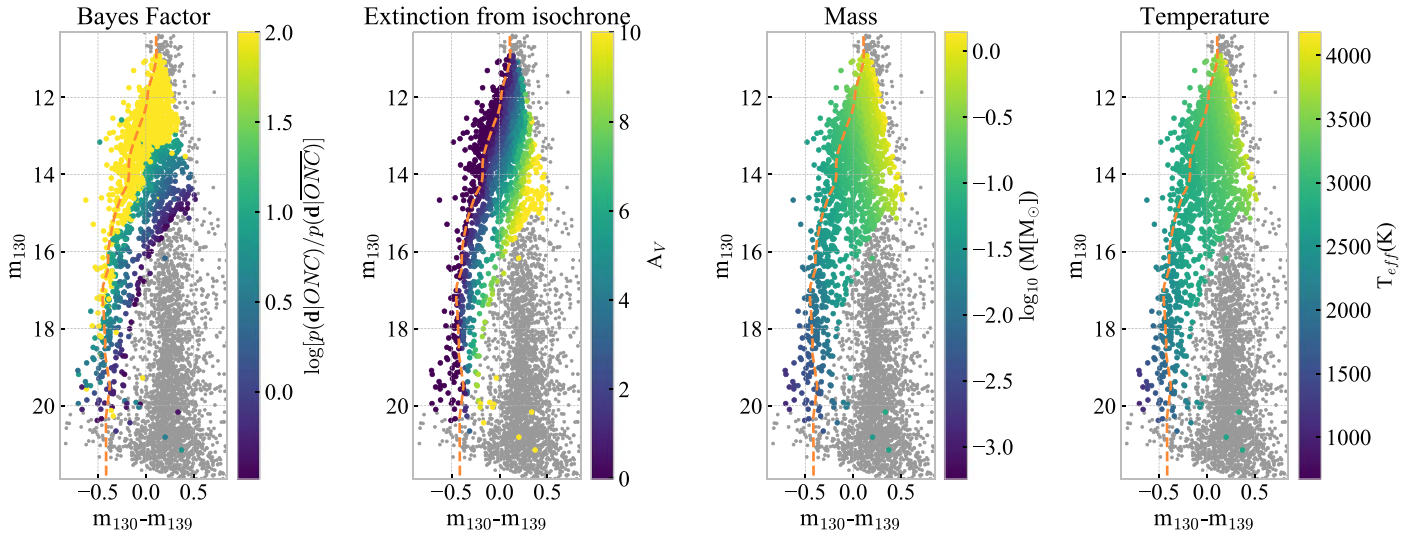

Figure 13. Gray dots at the faint end of the cluster population are due to the fact that, in our calculation of the Bayes factor, we apply a completeness cut at the faint end. Thus, for this faint-end sample below our completeness threshold we do not compute membership probabilities. The dashed orange line represents our semiempirical isochrone.

corresponds to logarithms of the Bayes factor >-0.5. Bona fide cluster members have Bayes factor >1. Our approach based solely on the H_2O CMD position of the objects represents a good first-order approach to the probability of ONC membership, especially on a global scale; it remains clear that for individual sources higher confidence can be reached when additional information (e.g., spectra or accurate proper motion) is available and taken into account.

4.11. Estimate of the Stellar Parameters

Having derived a bona fide empirical isochrone in our filters and a measure of the membership probability, we can try to deredden our candidates in the CMD to derive a raw estimate of their effective temperature and mass. We expect significant uncertainties in our derived stellar parameters. To begin with, the spread in luminosity discussed in Section 4.5 and other uncertainties result in a number of sources lying in the CMD above the empirical isochrone; their projection on the isochrone along the reddening vector requires unrealistic negative values for the extinction; we assign to them $A_V = 0$. For sources below the isochrone, we determine their A_V dereddening their photometry to the isochrone. As a result, the derived values of extinction can be quite different from those estimated through direct spectroscopic measurements. With these caveats, the results of our exercise are graphically shown in Figure 13 and presented in tabular form in Table 4. The list contains 1684 stars, having neglected all sources with $\log(\mathrm{BF}) < -0.5$ having probability larger than 80% of being contaminants and sources saturated according to the magnitude limits reported in Section 2.3. The extinction diagram shows the expected nearly vertical gradient along the reddening direction, with the largest $A_V \sim 15$ values reached by the more massive stars in the upper part of the diagram. The mass diagram shows that masses span the entire range from subsolar to a few Jupiter masses, while the temperatures range between about 4000 and 1500 K.

4.12. Ratio of Low-mass Stars to Brown Dwarfs

A parameterization often used in the literature to characterize the low-mass end of the IMF is the ratio R between stars and BDs. For the ONC, Andersen et al. (2011) investigated how R changes with the radial distance from the cluster center exploiting an HST/NICMOS survey (Robberto et al. 2013) covering ~28% of the region in J and H equivalent bands. After correction for field-star contamination, which they estimated at a 10% level for BDs down to a mass limit of 30 M_{Jup}, Andersen et al. (2011) found a cluster averaged value $R = 2.4$ with strong radial dependence, from $R = 7.2 \pm 5.6$ in an inner $d = 0.35$–0.7 pc annulus to $R = 1.1 \pm 0.8$ in the outer $d = 1.1$–1.5 pc annulus. If confirmed, a radial decrease of the ratio of stars to BDs could suggest that mass segregation can be traced down to the subsolar masses, or that BDs are already dynamically spread at $t \sim 1$ Myr, constraining the star formation history of the ONC. The reported uncertainties, however, are too large to draw conclusions. To put these R values in a more general context, one can refer, e.g., to Table 4 of Scholz et al. (2012), which lists the R values for eight young clusters. Their values range from $R = 2.3$ for NGC 1333, the object of their study, to $R = 8.3$ for IC 348, the value reported by Andersen et al. (2008). More recently, Mužić et al. (2019) found values in the range $R = 2$–5 for seven clusters. A solid confirmation of a spread in the R values for nearly coeval young clusters would also have major implications, pointing to variations of the IMF at substellar masses, but also in this case uncertainties are large.

If we adopt the same mass bins used by Andersen et al. (2011), i.e., 0.08–1.0 $M_\odot$ for the stars and 0.03–0.08 $M_\odot$ for BDs, we obtain R values that strongly depend on the Bayes factor, i.e., on our estimated membership probability (Table 5). Figure 14 shows the dependence of our R values versus the Bayes factor for the four radial zones of Andersen et al. (2011). In general, it is $R \simeq 6$–7 for Bayes factor ~2, our highest level of confidence. The dependence of R on the Bayes factor does not depend on the distance from the cluster center, with the possible exception of the outer region that shows a peak at Bayes factor ≃0, a feature caused by a relative increase of stellar contaminants versus BD contaminants for that R value.

Making a step further, in Figure 15 we present the corresponding R ratio for BD (0.015–0.08 $M_\odot$) versus planetary-mass objects (0.05–0.015 $M_\odot$). The spread of R

Table 5
Radial Dependence of the Number of ONC Sources

Radial Zone	Areal Coverage (arcsec^2)	Selection	Stars $0.08 \leqslant M < 1.00\,M_\odot$	Brown Dwarfs $0.015 \leqslant M < 0.03\,M_\odot$	Planetary-Mass Objects $0.005 \leqslant M < 0.015\,M_\odot$
$d \leqslant 0.35$ pc	328	Total	430	110	245
		Bayes factor = 2	300	46	25
$0.35 < d \leqslant 0.7$ pc	128	Total	311	85	405
		Bayes factor = 2	216	34	9
$0.7 < d \leqslant 1.1$ pc	1283	Total	268	73	703
		Bayes factor = 2	205	27	9
$d > 1.1$ pc	1983	Total	264	61	1453
		Bayes factor = 2	188	26	19

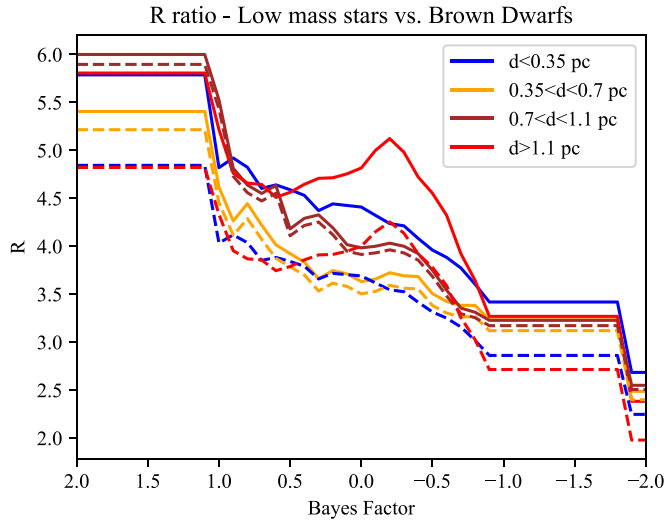

Figure 14. Star (0.08–1.0 $M_\odot$) to BD (0.03–0.08 $M_\odot$) ratio R vs. Bayes factor for the four radial zones indicated in the label. Solid lines refer to the observed counts, and dashed lines refer to the counts after completeness correction.

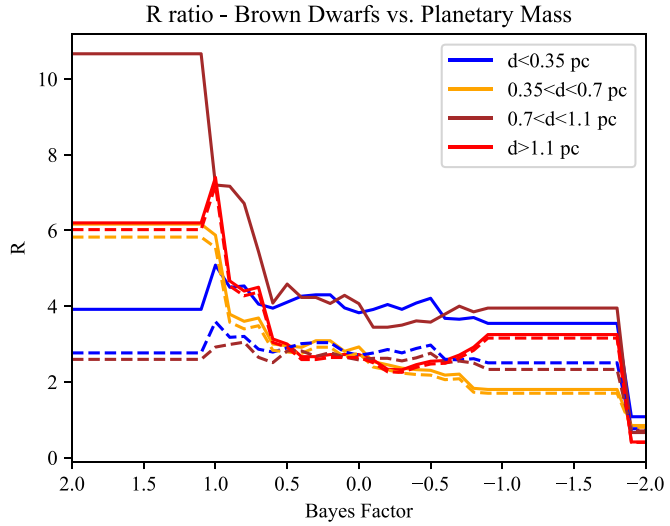

Figure 15. Same as Figure 14, but for the ratio of BD (0.03–0.08 $M_\odot$) to planetary-mass objects (0.005–0.03 $M_\odot$).

ratios for Bayes factor = 2 is larger, with a peak at $R \simeq 10$ for the 0.7 pc $< d <$ 1.1 pc region, but one has to take into account the low number of bona fide planetary-mass objects. After applying a completeness correction, we obtain R values

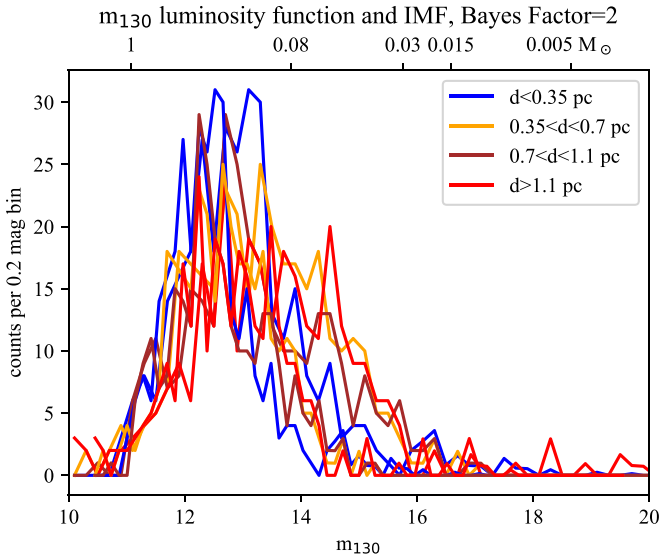

Figure 16. m_{130} luminosity function for our four radial regions centered on θ^1Ori-C, limited to our bona fide cluster members (Bayes factor = 2) and including completeness correction. The top axis indicates the corresponding stellar masses according to our 1 Myr isochrone.

in the range of 3–6, comparable to the star/BD ratio, and consistent with a steady decrease of the number of cluster members down to planetary masses (Béjar & Martín 2018).

If we use 0.072 and 0.012 $M_\odot$ as the hydrogen- and deuterium-burning mass limits, respectively, both values appropriate for solar metallicity, we count 136 BDs and 34 planetary-mass objects with Bayes factor = 2, i.e., bona fide members of the ONC. These numbers combined are comparable to the total number of known low-gravity L dwarfs (Béjar & Martín 2018; Burningham 2018), making our catalog one of the richest censuses to date of substellar and planetary-mass objects in a nearby star-forming region.

4.13. Luminosity and Initial Mass Function

In Figure 16 we present the m_{130} luminosity function, and the corresponding IMF, for our four radial regions centered on θ^1Ori-C, limited to our bona fide cluster members (Bayes factor = 2) and including completeness correction. The distribution, for all regions, peaks at $m_{130} \sim 12$–13, corresponding to about 0.4–0.2 $M_\odot$. The rapid decrease at $m_{130} < 12$ is due to our saturation limit. However, the decrease af fainter magnitudes, $m_{130} > 14$, in the substellar regime, is real.

In general, the discrepancy with, e.g., Andersen et al. (2011), i.e., our lower R ratio, can be reconciled if one accepts sources with low Bayes factor, in other words, if one increases the fraction of contaminants. These differences can thus be be regarded as just another proof of the difficulty of discriminating the true population of substellar and planetary-mass objects in the ONC from the reddened population of galactic and extragalactic contaminants using broadband photometry plus correction for field-star contamination. We defer to Paper II the detailed analysis of the low-mass IMF of the ONC.

5. Summary

We have carried out a Hubble Treasury Program (GO-13826) to determine a complete and unbiased census of the stellar population of the ONC down to a few Jupiter masses. To disentangle young substellar sources from the background galactic population and extragalactic sources, we have searched for the presence of H_2O vapor in absorption, a key signature of the atmosphere of substellar objects. Using the infrared channel of the Wide Field Camera 3 of the Hubble Space Telescope in the F139M and F130N filters, respectively corresponding to the 1.4 μm H_2O absorption feature and adjacent line-free continuum, we have built a spectral index sensitive to the presence and depth of atmospheric water vapor. We have detected 4504 sources down to magnitudes $\simeq$21.5–22, corresponding to masses $\sim$3 $M_{\rm Jup}$ for a 1 Myr isochrone at $\simeq$400 pc. About 742 sources, about 1/6 of the total, are fainter that $m_{130} = 14$ and have a negative F130M–F139N color index, indicative of the presence of H_2O vapor in absorption. These sources can be classified as bona fide M and L dwarfs, with temperatures $T \lesssim 2850$ K at an assumed 1 Myr cluster age. Their locus on the CMD is clearly distinct from the larger background population of highly reddened stars and galaxies with positive F130M–F139N color index. The faintest sources with H_2O absorption can be traced down to the sensitivity limit of our survey. We present the source photometry, an estimate of the main stellar parameters, and the membership probability based on a Bayesian analysis of our sample. The implications of our measures on the low-mass tail of the IMF, determined taking into account all ancillary information on the cluster structure, is presented in Paper II of this series.

Support for program No. GO-13826 was provided by NASA through a grant from the Space Telescope Science Institute, which is operated by the Association of Universities for Research in Astronomy, Incorporated, under NASA contract NASS-26555. C.F.M. acknowledges an ESO fellowship. The authors are indebted to an anonymous referee for useful comments and wish to thank Mike Meyer for reviewing an earlier version of the manuscript. This research has made use of the VizieR catalog access tool, CDS, Strasbourg, France. The original description of the VizieR service was published in Ochsenbein et al. (2000).

Facility: HST (WFC3).

Appendix A
BT-Settl Model Used in This Paper

The models adopted in this paper have been taken from the grids of the BT-Settl model available for download at https://phoenix.ens-lyon.fr/Grids/BT-Settl. They utilize the stellar theoretical isochrones of Baraffe et al. (2015) and the PHOENIX atmospheric model. The BT-Settl models, in particular, implement cloud formation and dust sedimentation in the atmospheres of BDs and planetary-mass objects. Since the library is subject to changes, we present in Table A1 the version we adopted, downloaded in 2016 October, limited to the passbands used in this paper. We also add, in the last two columns, the revised values of the F130N and F139M photometry according to the empirical ridgeline, derived as detailed in the following section.

To associate effective temperatures to spectral types, we adopt the parameterization provided by Luhman et al. (2003) for young M-type stars, whereas for L-type stars we adopt Faherty et al. (2016) for young moving groups deriving the values listed in Table A2.

Table A1
BT-Settl.M-0.0-HST-WFC3-1 Myr

$M/M_\odot$	$T_{\rm eff}$ (K)	$L/L_\odot$	log(g)	R (10^9 cm)	D	Li	m130N	m139M	m850LP$_1$	m850LP$_2$	m130N-RL	m139M-RL
0.0005	628	−5.37	2.65	12.25	1	1	17.559	23.253	21.667	21.69	19.731	20.137
0.001	942	−4.72	3	11.57	1	1	14.562	17.701	17.513	17.524	15.556	15.968
0.002	1285	−4.14	3.26	12.09	1	1	13.133	14.632	15.768	15.773	13.801	14.216
0.003	1553	−3.75	3.37	12.99	1	1	12.496	13.06	15.219	15.224	13.250	13.666
0.004	1747	−3.48	3.44	13.92	1	1	11.263	12.216	14.237	14.242	12.265	12.681
0.005	1901	−3.27	3.47	14.95	1	1	10.5	11.544	13.322	13.328	11.460	11.836
0.006	2004	−3.13	3.5	15.88	1	1	9.996	11.042	12.616	12.621	10.617	11.044
0.007	2098	−3	3.51	16.85	1	1	9.763	10.682	12.289	12.294	10.294	10.719
0.008	2159	−2.89	3.52	17.96	1	1	9.472	10.325	11.852	11.857	9.829	10.264
0.009	2207	−2.81	3.53	18.88	1	1	9.25	10.05	11.522	11.527	9.482	9.924
0.01	2251	−2.73	3.53	19.81	1	1	9.083	9.829	11.29	11.295	9.220	9.673
0.012	2321	−2.61	3.54	21.4	1	1	8.813	9.471	10.91	10.913	8.855	9.302
0.015	2400	−2.46	3.54	24.04	1	1	8.436	8.993	10.39	10.393	8.466	8.865
0.02	2484	−2.28	3.55	27.47	1	1	8.035	8.503	9.862	9.865	7.954	8.347
0.03	2598	−2.17	3.69	28.38	0.98	1	7.822	8.177	9.485	9.488	7.625	7.999
0.04	2746	−1.94	3.68	33.27	0.735	1	7.301	7.547	8.794	8.796	7.061	7.388
0.05	2768	−1.64	3.49	46.38	0.99	1	6.548	6.79	8.031	8.033	6.500	6.753
0.06	2824	−1.6	3.57	46.27	0.605	1	6.484	6.694	7.91	7.912	6.432	6.665
0.07	2853	−1.48	3.53	52.41	0.56	1	6.171	6.376	7.581	7.583	6.217	6.408
0.072	2858	−1.45	3.52	53.68	0.555	1	6.112	6.316	7.519	7.521	6.137	6.320

Table A1
(Continued)

$M/M_\odot$	$T_{\rm eff}$ (K)	$L/L_\odot$	log(g)	R (10^9 cm)	D	Li	m130N	m139M	m850LP$_1$	m850LP$_2$	m130N-RL	m139M-RL
0.075	2833	−1.39	3.46	58.93	0.915	1	5.94	6.158	7.375	7.377	6.002	6.179
0.08	2869	−1.37	3.49	58.47	0.51	1	5.907	6.111	7.311	7.313	5.939	6.115
0.09	2867	−1.29	3.46	64.54	0.4895	1	5.693	5.902	7.105	7.107	5.730	5.908
0.1	2856	−1.19	3.39	73.18	0.8	1	5.432	5.652	6.865	6.867	5.501	5.671
0.11	3023	−1.08	3.43	73.48	0.312	1	5.25	5.371	6.542	6.544	5.222	5.361
0.13	3072	−0.96	3.41	82.37	0.1975	1	4.948	5.046	6.222	6.223	4.955	5.055
0.15	3120	−0.85	3.39	90.05	0.112	1	4.708	4.779	5.957	5.958	4.732	4.801
0.175	3163	−0.76	3.39	97.57	0.0363	1	4.496	4.541	5.718	5.719	4.534	4.574
0.2	3193	−0.7	3.4	102.6	0.0041	1	4.361	4.389	5.56	5.561	4.405	4.424
0.25	3242	−0.61	3.43	110.47	0	1	4.16	4.163	5.326	5.327	4.201	4.198
0.3	3281	−0.53	3.46	118.1	0	1	3.982	3.966	5.125	5.126	4.016	4.001
0.35	3318	−0.46	3.47	125.44	0	1	3.82	3.787	4.944	4.945	3.844	3.823
0.4	3357	−0.39	3.48	132.28	0	1	3.672	3.623	4.779	4.78	3.696	3.662
0.45	3388	−0.34	3.49	138.4	0	1	3.548	3.486	4.64	4.641	3.575	3.528
0.5	3427	−0.28	3.5	144.06	0	1	3.437	3.353	4.508	4.509	3.463	3.402
0.57	3485	−0.21	3.52	151.93	0	1	3.293	3.174	4.33	4.331	3.311	3.231
0.6	3507	−0.17	3.52	155.92	0	1	3.224	3.094	4.25	4.251	3.242	3.154
0.62	3525	−0.15	3.52	157.89	0	1	3.182	3.048	4.2	4.201	3.198	3.106
0.7	3593	−0.08	3.53	164.8	0	1	3.036	2.887	4.026	4.027	3.042	2.936
0.75	3632	−0.04	3.54	169.47	0	1	2.945	2.789	3.919	3.92	2.939	2.831
0.8	3670	0	3.55	173.8	0	1	2.862	2.701	3.821	3.822	2.844	2.733
0.85	3705	0.04	3.55	178.34	0	1	2.78	2.613	3.726	3.727	2.748	2.638
0.9	3752	0.03	3.61	171.83	0	1	2.823	2.654	3.748	3.749	2.771	2.660
0.95	3776	0.11	3.56	186.04	0	1	2.633	2.461	3.555	3.556	2.574	2.466
1	3810	0.13	3.58	187.82	0	1	2.586	2.412	3.495	3.496	2.514	2.406
1.05	3841	0.17	3.57	193.6	0	1	2.497	2.322	3.396	3.397	2.415	2.307
1.1	3871	0.21	3.57	197.99	0	1	2.425	2.25	3.314	3.315	2.331	2.225
1.15	3899	0.23	3.58	201.14	0	1	2.369	2.193	3.248	3.248	2.262	2.158
1.2	3978	0.28	3.58	203.89	0	1	2.28	2.104	3.136	3.136	2.145	2.044
1.3	4098	0.35	3.6	208.83	0	1	2.141	1.967	2.962	2.963	1.952	1.865
1.4	4197	0.42	3.6	214.98	0	1	2.006	1.836	2.797	2.797	1.754	1.691

Note. Version Oct. 2016.

Table A2
Spectral Type vs. Effective Temperature Relation According to Faherty et al. (2016)

Spectral Type	$T_{\rm eff}$(K)
L0	2173
L1	1983
L2	1809
L3	1649
L4	1504

Appendix B
Empirical Ridgeline

In this appendix we describe the process leading to our empirical isochrone, i.e., a mean locus in our near-IR CMD where all our observations would, on average, lie after extinction correction. We refer to this locus as the ridgeline. Several factors have to be taken into account to build a ridgeline that can be compared to a theoretical isochrone, namely, membership, differential extinction, distance, binaries, and photometric errors.

Membership.—Using our CMD, it is easy to separate the majority of low-mass members of the ONC from background stars. We trace a line in the CMD that approximately follows the distribution of ONC sources, shifted to bluer colors to separate the large population of objects that clearly stand out as nonmembers (Figure B1, left panel). We shall only consider in our subsequent analysis the objects that fall within the area indicated in Figure B2. This leaves us with 1830 sources. The edges of the segmented line defining the region are given in Table B1.

Accounting for Differential Extinction.—Given our assumption that the discrepancy between models and data is intrinsic to the atmosphere treatment, it is preferable to derive the correction in the CMD of absolute magnitudes. In order to do this, we have to subtract the extinction in each band from the photometry of our sources. Scandariato et al. (2011) derived a map of the extinction in the region. We use their map to remove extinction with two caveats. First, we have to assume a reddening law to connect the A_V from the map to the extinction in each band. We use the Cardelli et al. (1989) law, with $R_V = 3.1$, and the relations for A_{130}/A_V and A_{139}/A_V presented in Equation (1) and (2). Second, the A_V values from Scandariato et al. (2011) are spatial averages over an area of few square arcminutes. To assume for all nearby sources the same average extinction would ignore the scatter between individual sources present in the original data. Therefore, we draw instead an A_V value for each source from a lognormal

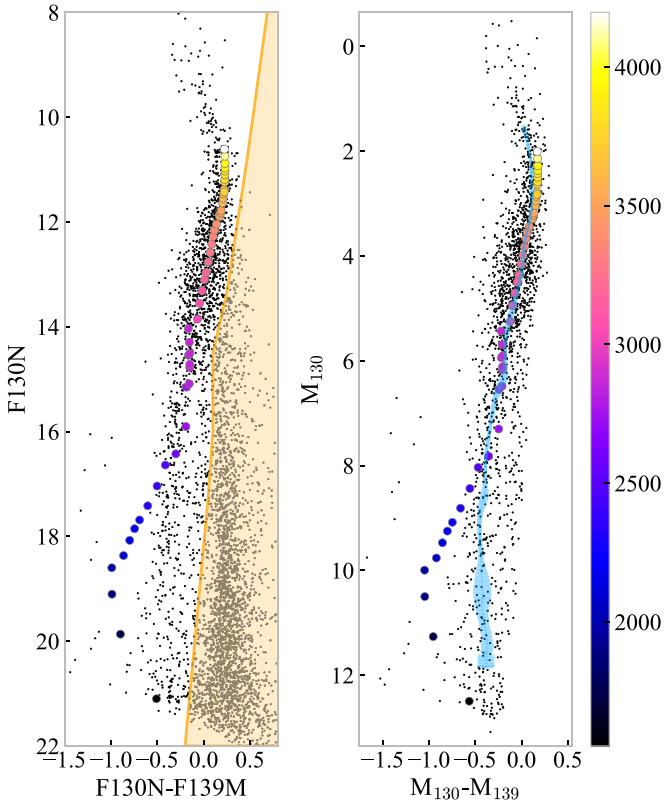

Figure B1. Left: our near-IR CMD, with a 1 Myr isochrone superimposed at a distance of 403 pc reddened assuming the median visual extinction of the cluster members ($A_V = 2.18$) as derived from the Scandariato et al. (2011) map, and assuming $A_{130}/A_V = 0.264$ and $A_{139}/A_V = 0.241$. The orange area defines the exclusion region for background objects. Right: absolute magnitudes ($d = 10$ pc) and colors of the stars considered as members, and the 1 Myr isochrone without reddening. The blue stripe represents the empirical ridgeline, with variable thickness representing its 1σ uncertainty. The dots describing the isochrone are color-coded according to the linear effective temperature scale shown at the right side of the figure.

Table B1
Edges of the Segmented Line Describing the Exclusion Limit for Background Sources

$m_{130}-m_{139}$	m_{130}
1	4
0.47	10.80
0.25	13.35
0.1	14.5
0.1	16.0
0.05	17.25
−0.2	22

Note. Sources redder than the segmented line in the table are considered background for the purpose of defining the empirical ridgeline.

distribution. The (μ, σ) parameters of the distribution are set to

$$\mu = \log(A_{V,\mathrm{map}}) - 0.5\log(1+\alpha^2) \quad \text{(B1)}$$

$$\sigma = \sqrt{\log(1+\alpha^2)}, \quad \text{(B2)}$$

where $A_{V,\mathrm{map}}$ is the extinction value from the Scandariato et al. (2011) map at the position of that source. The lognormal distribution arises naturally when describing the column density distribution of the turbulent interstellar medium (ISM; Kritsuk et al. 2007), and we thus use it to parameterize the distribution of extinction. The parameter α is equal to the ratio between the standard deviation and the mean of the distribution; thus, an α of 0.1 means that the distribution's width is about 10% of the distribution mean. We adopt $\alpha = 0.3$, which in turn gives $\sigma = 0.29$, similar to what is expected from ISM simulations (see Kritsuk et al. 2017).

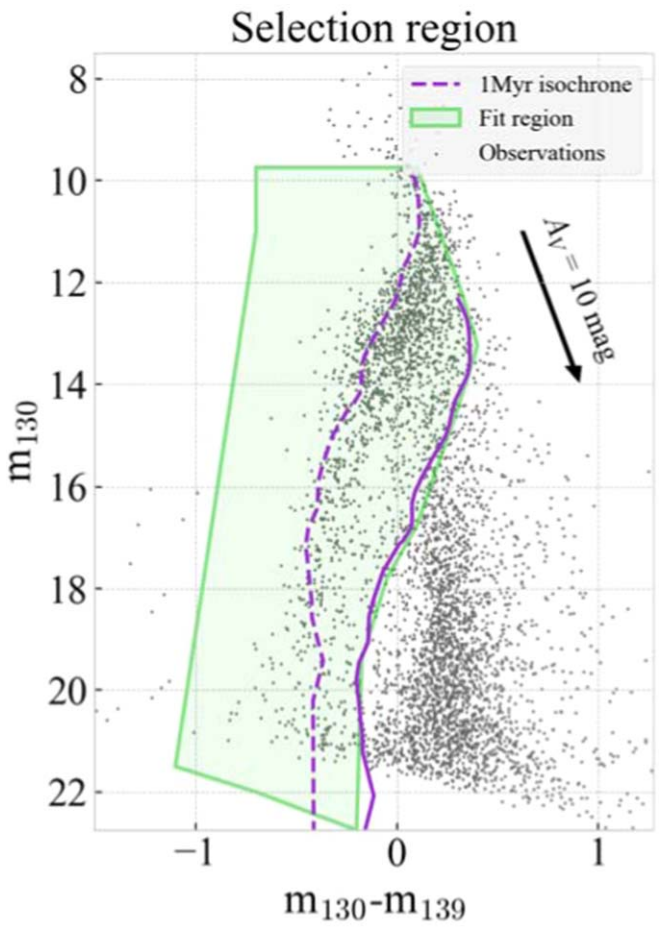

Figure B2. Illustration of the area used to determine an extinction-limited sample of low-mass members of the ONC.

Distance.—As described above for the extinction, distance needs to be accounted for in order to compare data and models in absolute magnitudes. For the ONC we adopt a distance of 403 pc, on the basis of Gaia DR2 data and APOGEE-2 near-IR spectroscopy (Kounkel et al. 2017; Getman et al. 2019). A recent estimate by Kounkel et al. (2017), based on Gaia DR2 data and APOGEE-2 near-IR spectroscopy, provides a slightly shorter distance, 386 ± 3 pc. For comparison, Slesnick et al. (2004) assumed 480 pc, while da Rio et al. (2012) adopted $d = 414 \pm 7$ pc from Menten et al. (2007). The recent studies utilizing GAIA data seem to confirm a distance close to 400 pc, and their discrepancy translates to a systematic uncertainty of ≃0.05 mag, irrelevant for our discussion.

Binaries.—Given a set of points in a CMD, the method for computing the ridgeline is described in Correnti et al. (2016). These authors describe how such a method is able to trace the mode of the population, and it is not affected by the presence of the "parallel sequence" of binaries that could bias the ridgeline construction.

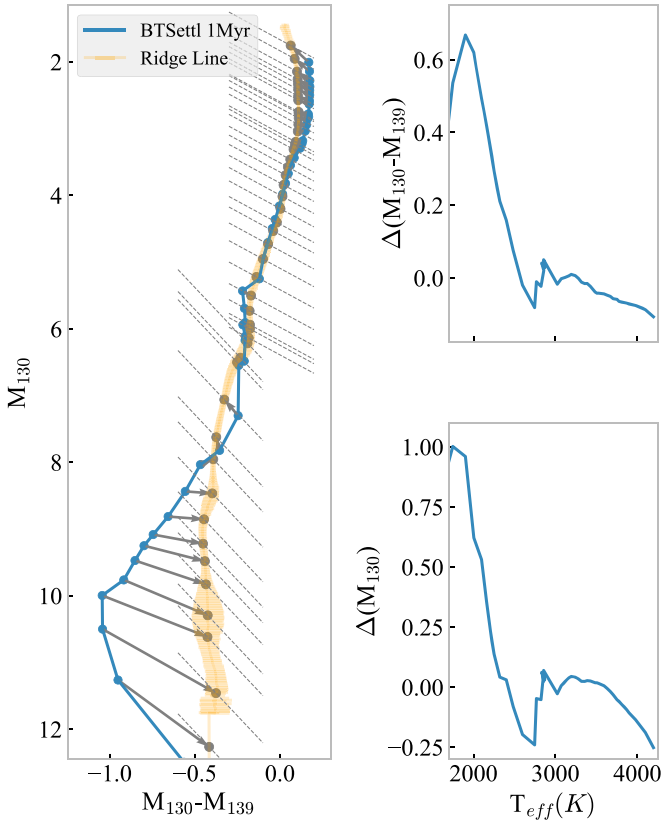

Figure B3. Left: empirical correction for each point along the isochrone. The dashed lines correspond to the constraints from the color–color diagram, Equation (4). Each point on the isochrone is shifted, to meet the gray points that represent the intercept between its constraint line (based on the above equations, for the F850LP value corresponding to that point) and the ridgeline. Right: resulting shifts in color (top panel) and magnitude (bottom panel) as a function of the temperature along the isochrone.

Photometric Errors.—We account for the effect of photometric errors on the description of the ridgeline by bootstrapping a set of catalogs, each of which contains the same number of stars as the original catalog members (i.e., the objects outside the orange region of Figure B1, left).

Single Iteration.—We create a catalog by first creating a bootstrapped list of 1830 sources, the number of nonbackground sources that may be preliminarily associated with the cluster population. This means that we extract 1830 sources among the 1830 existing ones, allowing for repetitions. We then subtract from each observed data point the distance modulus, extract a random value for its A_V from the individual lognormal distributions described above, and subtract the extinction in each band. We then obtain a single-iteration ridgeline from this catalog using the method described in detail in Correnti et al. (2016).

The method consists of estimating the source density in the CMD using a kernel density estimation. We then find the maximum of such a density distribution (the peak of this ragged density landscape) and move along the direction of minimum gradient, thus tracing the ridge.

Final Step.—We repeat the process for 5000 bootstrapped catalogs. At each iteration, different sources may be present in the catalog, and every time a source is present, it has a different random value of the extinction. At each iteration, the ridgeline will be slightly different, thus accounting for all the uncertainties above.

We combine the results of the 5000 iterations by binning the points from the ensemble of ridge lines in m_{130} absolute magnitude bins. We derive the average color of the combined ridgeline as a function of magnitude. We also derive the ridgeline color error, i.e., the standard deviation of the color distribution within each bin. The result is shown in the right panel of Figure B1.

B.1. Empirical Isochrone

Having determined the ridgeline, we can derive the correction needed to adjust the theoretical isochrone to the data. For each mass value along the 1 Myr BT-Settl isochrone we use the appropriate version of Equation (4), according to whether the mass is smaller or larger than 0.07 $M_\odot$. We then use the corresponding value of m_{850} for that mass, to derive a straight line in the m_{130} versus (m_{130}−m_{139}) CMD. We find the intercept between this straight line and the ridgeline; the intercept satisfies both constraints set by the color–color diagram (i.e., the $A_V = 0$ lower envelope) and by the CMD ridgeline. In terms of absolute magnitudes, we determine the shift in M_{130} and $M_{130} - M_{139}$ color needed to move the point on the theoretical isochrone, for the mass in question, toward the corresponding dual-constraint point in the CMD. We repeat this for all masses along the isochrone. Finally, we linearly interpolate the shifts in magnitude and color as a function of the effective temperature along the 1 Myr BT-Settl isochrone and derive empirical corrections, ($\Delta_{M_{130}}$, $T_{\rm eff}$) and ($\Delta_{M_{130}-M_{139}}$, $T_{\rm eff}$). The process is illustrated in Figure B3.

ORCID iDs

Massimo Robberto https://orcid.org/0000-0002-9573-3199
Mario Gennaro https://orcid.org/0000-0002-5581-2896
Maria Giulia Ubeira Gabellini https://orcid.org/0000-0002-5980-4287
Camilla Pacifici https://orcid.org/0000-0003-4196-0617
Morten Andersen https://orcid.org/0000-0002-5306-4089
Travis Barman https://orcid.org/0000-0002-7129-3002
Andrea Bellini https://orcid.org/0000-0003-3858-637X
Selma E. de Mink https://orcid.org/0000-0001-9336-2825
Giuseppe Lodato https://orcid.org/0000-0002-2357-7692
Carlo Felice Manara https://orcid.org/0000-0003-3562-262X
Imants Platais https://orcid.org/0000-0003-2599-2459
Laurent Pueyo https://orcid.org/0000-0003-3818-408X
Giovanni Maria Strampelli https://orcid.org/0000-0002-1652-420X
Jonathan C. Tan https://orcid.org/0000-0002-3389-9142
L. Testi https://orcid.org/0000-0003-1859-3070

References

Abel, N. P., Ferland, G. J., & O'Dell, C. R. 2019, ApJ, 881, 130
Ackerman, A. S., & Marley, M. S. 2001, ApJ, 556, 872
Andersen, M., Meyer, M. R., Greissl, J., & Aversa, A. 2008, ApJL, 683, L183
Andersen, M., Meyer, M. R., Robberto, M., Bergeron, L. E., & Reid, N. 2011, A&A, 534, A10
Bally, J., O'Dell, C. R., & McCaughrean, M. J. 2000, AJ, 119, 2919
Baraffe, I., Homeier, D., Allard, F., & Chabrier, G. 2015, A&A, 577, A42
Béjar, V. J. S., & Martín, E. L. 2018, in Handbook of Exoplanets, ed. H. J. Deeg & J. A. Belmonte (New York: Springer), 92
Bouy, H., Alves, J., Bertin, E., Sarro, L. M., & Barrado, D. 2014, A&A, 564, A29
Burningham, B. 2018, in Handbook of Exoplanets, ed. H. J. Deeg & J. A. Belmonte (New York: Springer), 118
Burrows, A., Sudarsky, D., & Lunine, J. I. 2003, ApJ, 596, 587
Cardelli, J. A., Clayton, G. C., & Mathis, J. S. 1989, ApJ, 345, 245
Chabrier, G., & Baraffe, I. 2000, ARA&A, 38, 337
Cook, N. J., Scholz, A., & Jayawardhana, R. 2017, AJ, 154, 256

Correnti, M., Gennaro, M., Kalirai, J. S., Brown, T. M., & Calamida, A. 2016, ApJ, 823, 18
da Rio, N., Robberto, M., Hillenbrand, L. A., Henning, T., & Stassun, K. G. 2012, ApJ, 748, 14
da Rio, N., Robberto, M., Soderblom, D. R., et al. 2010, ApJ, 722, 1092
da Rio, N., Tan, J. C., Covey, K. R., et al. 2016, ApJ, 818, 59
Dalcanton, J. J., Williams, B. F., Lang, D., et al. 2012, ApJS, 200, 18
Delfosse, X., Tinney, C. G., Forveille, T., et al. 1999, A&AS, 135, 41
Dolphin, A. E. 2000, PASP, 112, 1383
Drass, H., Haas, M., Chini, R., et al. 2016, MNRAS, 461, 1734
Dressel, L. 2014, Wide Field Camera 3 Instrument Handbook (Baltimore, MD: STScI), https://hst-docs.stsci.edu/wfc3ihb
Eisner, J. A., Bally, J. M., Ginsburg, A., & Sheehan, P. D. 2016, ApJ, 826, 16
Faherty, J. K., Riedel, A. R., Cruz, K. L., et al. 2016, ApJS, 225, 10
Gennaro, M., & Robberto, M. 2020, ApJ, 896, 80
Getman, K. V., Feigelson, E. D., Kuhn, M. A., & Garmire, G. P. 2019, MNRAS, 487, 2977
Gorlova, N. I., Meyer, M. R., Rieke, G. H., & Liebert, J. 2003, ApJ, 593, 1074
Großschedl, J. E., Alves, J., Meingast, S., et al. 2018, A&A, 619, A106
Herbst, W., Bailer-Jones, C. A. L., Mundt, R., Meisenheimer, K., & Wackermann, R. 2002, A&A, 396, 513
Hillenbrand, L. A., & Carpenter, J. M. 2000, ApJ, 540, 236
Hillenbrand, L. A., Hoffer, A. S., & Herczeg, G. J. 2013, AJ, 146, 85
Husser, T. O., Wende-von Berg, S., Dreizler, S., et al. 2013, A&A, 553, A6
Ingraham, P., Albert, L., Doyon, R., & Artigau, E. 2014, ApJ, 782, 8
Jeffries, R. D., Littlefair, S. P., Naylor, T., & Mayne, N. J. 2011, MNRAS, 418, 1948
Jones, H. R. A., Longmore, A. J., Jameson, R. F., & Mountain, C. M. 1994, MNRAS, 267, 413
Kirkpatrick, J. D., Reid, I. N., Liebert, J., et al. 1999, ApJ, 519, 802
Koekemoer, A. M., Faber, S. M., Ferguson, H. C., et al. 2011, ApJS, 197, 36
Kong, S., Arce, H. G., Feddersen, J. R., et al. 2018, ApJS, 236, 25
Kounkel, M., Covey, K., Suárez, G., et al. 2018, AJ, 156, 84
Kounkel, M., Hartmann, L., Loinard, L., et al. 2017, ApJ, 834, 142
Krist, J. E., Hook, R. N., & Stoehr, F. 2011, Proc. SPIE, 8127, 81270J
Kritsuk, A. G., Norman, M. L., Padoan, P., & Wagner, R. 2007, ApJ, 665, 416
Kritsuk, A. G., Ustyugov, S. D., & Norman, M. L. 2017, NJPh, 19, 065003
Kroupa, P. 2001, MNRAS, 322, 231
Kuhn, M. A., Hillenbrand, L. A., Sills, A., Feigelson, E. D., & Getman, K. V. 2019, ApJ, 870, 32
Lada, C. J., & Lada, E. A. 2003, ARA&A, 41, 57
Laidler, V. 2008, Synphot Data User's Guide (Baltimore, MD: STScI), http://stsdas.stsci.edu/stsci_python_epydoc/hst_synphot.pdf
Lucas, P. W., Roche, P. F., & Tamura, M. 2005, MNRAS, 361, 211
Luhman, K. L., Stauffer, J. R., Muench, A. A., et al. 2003, ApJ, 593, 1093
Manara, C. F., Robberto, M., da Rio, N., et al. 2012, ApJ, 755, 154
Menten, K. M., Reid, M. J., Forbrich, J., & Brunthaler, A. 2007, A&A, 474, 515
Mohanty, S., Basri, G., & Jayawardhana, R. 2005, AN, 326, 891
Morales-Calderón, M., Stauffer, J. R., Stassun, K. G., et al. 2012, ApJ, 753, 149
Morgan, W. W., Keenan, P. C., & Kellman, E. 1943, An Atlas of Stellar Spectra, with an Outline of Spectral Classification (Chicago, IL: Univ. Chicago Press)
Morley, C. V., Marley, M. S., Fortney, J. J., et al. 2014, ApJ, 787, 78
Muench, A., Getman, K., Hillenbrand, L., & Preibisch, T. 2008, in Handbook of Star Forming Regions I, ed. B. Reipurth (Tucson, AZ: Univ. Arizona Press), 483
Muench, A. A., Lada, E. A., Lada, C. J., & Alves, J. 2002, ApJ, 573, 366
Mužić, K., Scholz, A., Peña Ramírez, K., et al. 2019, ApJ, 881, 79
Najita, J. R., Tiede, G. P., & Carr, J. S. 2000, ApJ, 541, 977
Ochsenbein, F., Bauer, P., & Marcout, J. 2000, A&AS, 143, 23
O'Dell, C. R., Muench, A., Smith, N., & Zapata, L. 2008, in Handbook of Star Forming Regions I, ed. B. Reipurth (Tucson, AZ: Univ. Arizona Press), 544
O'dell, C. R., & Wong, K. 1996, AJ, 111, 846
Pacifici, C., Kassin, S. A., Weiner, B. J., et al. 2016, ApJ, 832, 79
Portegies Zwart, S. F., McMillan, S. L., & Gieles, M. 2010, ARA&A, 48, 431
Reggiani, M., Robberto, M., da Rio, N., et al. 2011, A&A, 534, A83
Ricci, L., Robberto, M., & Soderblom, D. R. 2008, AJ, 136, 2136
Riddick, F. C., Roche, P. F., & Lucas, P. W. 2007, MNRAS, 381, 1077
Robberto, M., Soderblom, D. R., Bergeron, E., et al. 2013, ApJS, 207, 10
Robberto, M., Song, J., Mora Carrillo, G., et al. 2004, ApJ, 606, 952
Robin, A. C., Reylé, C., Derrière, S., & Picaud, S. 2003, A&A, 409, 523
Ruffio, J.-B., Mawet, D., Czekala, I., et al. 2018, AJ, 156, 196
Scandariato, G., Robberto, M., Pagano, I., & Hillenbrand, L. A. 2011, A&A, 533, A38
Scholz, A., Muzic, K., Geers, V., et al. 2012, ApJ, 744, 6
Slesnick, C. L., Hillenbrand, L. A., & Carpenter, J. M. 2004, ApJ, 610, 1045
Smith, R. M., Zavodny, M., Rahmer, G., & Bonati, M. 2008, Proc. SPIE, 7021, 70210J
Strampelli, M. G., Aguilar, J., Pueyo, J., et al. 2020, ApJ, 896, 81
Wallace, L., Meyer, M. R., Hinkle, K., & Edwards, S. 2000, ApJ, 535, 325
Weights, D. J., Lucas, P. W., Roche, P. F., Pinfield, D. J., & Riddick, F. 2009, MNRAS, 392, 817